1.08 Theory and Observations - Seismology and the Structure of the Earth: Teleseismic Body-Wave Scattering and Receiver-Side Structure

MG Bostock, The University of British Columbia, Vancouver, BC, Canada

1.08.1 Introduction

The analysis of scattered, teleseismic body waves to characterize the receiver-side lithosphere and upper mantle spans over 4 decades, and it is now among the most widely used means of resolving fine-scale structure in these outer layers of the Earth. The first studies to harness converted teleseismic waves for investigation of deep Earth structure were undertaken in the former Soviet Bloc (Rainer Kind, pers. comm; see, e.g., Hoffmann et al., 1989). Most early studies involved single-station analyses, and the work of Phinney (1964) represents an important milestone. He recognized that one could remove the effect of the earthquake source by examining spectral ratios of radial and vertical component *P*-seismograms measured at a surface receiver and thereby gain insight into the bulk properties of the Earth's crust. His work was formulated in the frequency domain (see also Kurita, 1973) and constitutes the first application of the so-called receiver function technique. Soon thereafter, Båth and Stefánson (1966) examined recordings of teleseismic *S* and identified *S*-to-*P* precursors scattered from the crust–mantle boundary as a viable means once again of characterizing crustal structure. A full decade was to elapse before the next major development. Working independently on transition zone and crustal structure, respectively, Vinnik (1977) and Langston (1979) introduced the time-domain, *P* receiver function to characterize receiver-side *P*-to-*S* conversions present within the coda of teleseismic *P*. The time-domain receiver function, which contains information on phase, has intuitive appeal as a leading-order approximation to the Earth's Green function at early times (i.e., up until the arrival of the next major phase *PP*). In addition, Vinnik (1977) enhanced the weak scattered signals present in the receiver function by stacking multiple receiver functions from different epicentral distance ranges along theoretical move-out curves for a radial Earth model, thereby effectively approximating a 1-D, single-scattering inversion. By the mid-1980s, an increasing number of researchers had come to recognize the potential of the approach in general applications (e.g., Kind and Vinnik, 1988; Owens et al., 1984; Zandt and Owens, 1986). This recognition combined with the growing availability of three-component, broadband seismometers and high-capacity, digital acquisition systems has led to the popularity that teleseismic receiver function analysis enjoys today in regional studies of lithospheric and upper mantle structure.

In the last decade, there has been major focus on placing the empirical 'receiver function' technique on a firmer theoretical foundation and extending its application to multichannel data sets. In both respects, much has been (and may still be) learned from the vast, accumulated experience in exploration seismology. Although geometries in the global and exploration contexts are at first glance quite different (plane-wave excitation from below versus point source excitation from above), both disciplines share an important common element, namely, the interaction of near-vertically propagating waves with near-horizontal and, often, modest-contrast stratification. The recorded wave fields are thus free of postcritical interactions that lead to dispersive, guided waves and can be inverted to extract highly resolved information on subsurface material property contrasts within a single-scattering (or 'Born approximation') framework. Nonetheless, there are important distinctions between the two disciplines. Exploration seismology has, for practical reasons (source

generation and recording), largely ignored elastic phenomena by focusing on pure *P*-mode scattering and modeling data with acoustic theory. Global seismology, in contrast, relies primarily on conversions to resolve subsurface structure, and pure-mode reflections have, to date, played a far lesser role. It is interesting to note that the two communities have begun to forge closer links (e.g., Marfurt et al., 2003) due in part to the growing interest in exploration for the use of local, passive seismicity to monitor changes in hydrocarbon reservoirs.

In this chapter, we will provide an overview of the theory that underlies the processing of scattered teleseismic wave fields and thereby facilitates interpretation for regional lithospheric and upper mantle structure. Section 1.08.2 begins with a description of the geometric attributes of different teleseismic phases that can be considered for use in studies of the lithosphere and upper mantle, along with their merits and shortcomings. The canonical problem of structural response/source signature separation is then addressed in the teleseismic context. This discussion centers on the relationship between the classic receiver function and the more fundamental Green function that is required in formal inverse-scattering approaches. Sections 1.08.4 and 1.08.5 examine the inverse problem for one- and multidimensional heterogeneity. The focus here is on formal inverse-scattering techniques because of the insight they afford into physics of the scattering process and because they provide a framework through which more empirical schemes can be understood. In the final section, we discuss several shortcomings arising from the single-scattering or Born approximation that has, to this point, underlain most attempts to invert scattered teleseismic body waves for receiver-side structure. We then sketch out a means through which nonlinear inverse scattering could, in principle, be applied to teleseismic wave fields, based on recent theoretical developments in exploration seismology. Before proceeding, we mention several additional review sources that the reader may wish to consult in gaining a broader appreciation for the field, namely, Pavlis (2005), which discusses outstanding issues in the inversion of teleseismic *P*-wave fields for receiver-side structure; Rondenay (2009), which provides a survey of upper mantle imaging studies using scattered waves; and Kennett (2002), a more general treatise of observational seismology at regional scales that includes a chapter on teleseismic body-wave fields.

1.08.2 Geometrical Preliminaries

In this section, we sketch out the general scattering geometry to be considered for the remainder of the chapter. We shall restrict our attention to incident-wave fields representing sources located at teleseismic distances (i.e., epicentral distance $\Delta > 30°$) from one or more receivers located at the Earth's surface. The term 'incident-wave field' will be defined more precisely in later sections, but for the present, it can be considered to be the signal associated with a primary body-wave phase that has reflected/converted, if at all, only at the Earth's surface and/or core–mantle boundary, for example, *P*, *pP*, *PP*, *S*, *pS*, *PKP*, *SKS*, and *ScS* (see Figure 1). This definition serves to distinguish the incident-wave field from the scattered waves generated through reflection or mode conversion at receiver-side heterogeneity that we are ultimately interested in exploiting

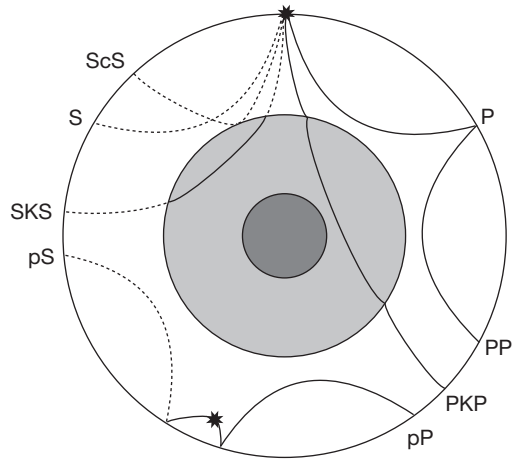

Figure 1 Ray paths of some major phases referred to in text that may serve as incident-wave fields for study of near-receiver scattering from subsurface structure (*P*-wave legs, solid; *S*-wave legs, dashed).

(Burdick and Langston, 1977). Signals originating through source-side scattering will, in contrast, be most conveniently treated as part of the source signature.

For much of what follows, we shall focus our attention on teleseismic *P* as it historically has been the most practically useful of the candidate incident-wave fields and ignore, for the moment, associated depth phases created by deep earthquakes. At lesser distances ($14° < \Delta < 30°$), *P* (and *S*) waves traveling through the mantle experience triplications at strong velocity gradients defining the Earth's transition zone (between ~400 and 670 km depth), and consequently, the incident-wave field will comprise several superposed arrivals characterized by different horizontal slownesses that are difficult to distinguish and separate (see Figure 2 and, e.g., Kennett, 2002). In the distance range $30° < \Delta < 100°$, teleseismic *P* bottoms within the lower mantle, which is generally characterized by a smoothly varying and dominantly radial velocity profile. Consequently, propagation is simple and the wave field is accurately modeled by a single surface slowness that decreases monotonically from ~0.08 to 0.04 s km^{-1} (or, equivalently, through ray parameters of 8.8 to 4.4 s per degreee) over this distance range. Moreover, wave front curvature is small because we are well into the far field, and it is frequently convenient in both single-station and multistation applications to approximate the incident teleseismic wave field as planar in horizontal aspect (see, e.g., Section 1.08.3.1). The small values of horizontal slowness also manifest steep angles of propagation that are, again, advantageous in that the likelihood of postcritical interactions is reduced. Complications due to depth phases can be dealt with in two ways, depending on source depth. As depth decreases, the slowness (and timing) of the depth phases approach that of the incident-wave field such that they can be considered one and the same. At greater depths, the difference in slowness may be significant, but in this case, the short duration of time functions that characterize the Wadati–Benioff sources combined with greater time separation between the incident-wave field and depth phases will usually permit the depth phases to be temporally windowed and analyzed independently. The source depth at which one

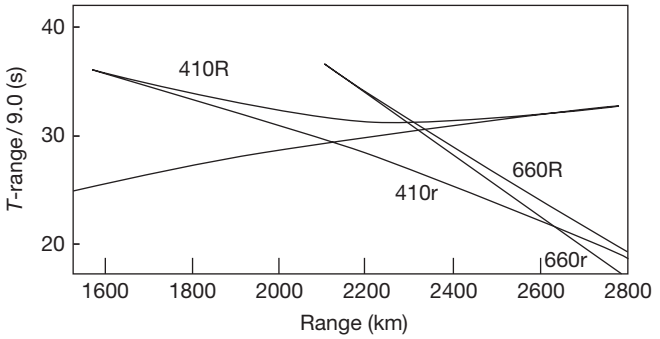

Figure 2 Travel-time curves at regional distances displaying triplications due to transition zone (410 and 660 km) discontinuities that complicate analysis of scattering from more shallow discontinuities. Individual travel-time branches are labeled by the associated discontinuity (*r*, refraction; *R* reflection).

draws the line between inclusion and separation of depth phases will depend on the application but will generally be taken to lie between 100 and 200 km.

The treatment of teleseismic *S* is somewhat more difficult than teleseismic *P* for a number of reasons. First, the distance range over which useful recordings can be procured is more limited. This is due in part to the development of postcritical *S*-to-*P* conversion from deeper (e.g., transition zone) discontinuities at larger slowness. In addition, conversion and triplication at the core–mantle boundary lead to close coincidence and interference of *S*, *SKS*, and *ScS* over the distance range 70–90°. Depending on source mechanism, all three *S* phases may possess comparable amplitudes, and their separation (and that of associated scattered fields) is difficult, especially where three-dimensional heterogeneity is expected. *SKS* extends the usable distance range well beyond 100°, but the number of high signal-to-noise ratio recordings diminishes rapidly with distance. Second, because teleseismic *S* is characterized by larger slowness than teleseismic *P* at any given epicentral distance, postcritical phenomena within the receiver-side crust occur at smaller epicentral distances (*Spdp* (Zandt and Randall, 1985) and shear-coupled *PL* (Baag and Langston, 1985; Frazer, 1977; Owens and Zandt, 1997)) that can complicate interpretation and inversion. Third, the receiver-side response to an incident *S*-wave field will generally depend on the wave field polarization as imparted by the source and modified by source-side heterogeneity/anisotropy. The incident polarization is not generally known (with the exception of *SKS* that is radially polarized due to receiver-side conversion from *P* to *S* at the core–mantle boundary), though its influence can under certain assumptions be removed (e.g., Farra and Vinnik, 2000; **Section 1.08.3.4**). Fourth, higher frequencies in teleseismic *S* (and hence its resolving power) are attenuated more severely than those in teleseismic *P* due to lower *Q* especially in the shallow upper mantle. Lastly, signal-generated noise levels are generally higher in teleseismic *S* due to the energy that has propagated some large portion of its path as *P* (Bock, 1994; Vinnik and Romanowicz, 1991; Wilson et al., 2006). Although it might be argued that free-surface multiples arriving as *S*-waves in the coda of teleseismic *P* represent a comparable form of signal-generated noise exacerbating interpretation of direct *P*-to-*S* conversions, these multiples are generated by receiver-side heterogeneity and can be exploited to leverage additional and complementary constraint on structure (see **Sections 1.08.4.3** and **1.08.5**).

Despite these complications, there has been renewed interest in recent years in teleseismic *S*-to-*P* conversions as means of characterizing the lithosphere to asthenosphere boundary (e.g., Kawakatsu et al., 2009; Kumar et al., 2005; Li et al., 2004; Oreshin et al., 2002; Rychert et al., 2007; Vinnik et al., 2005; Yuan et al., 2006). The growing waveform archive afforded by the profusion of modern digital networks has enabled stacking of large quantities of data to mitigate the low signal-to-noise ratios that characterize these phases, resulting in important new insights into this enigmatic structure (Eaton et al., 2009; Rychert et al., 2010).

The utility of most other phases is still more limited due to either interference or low signal-to-noise levels, although it is often used to augment teleseismic *P* data *PP* (e.g., Gurrola et al., 1994; Owens et al., 2000). Useful structural information has on occasion also been extracted from regional *P* (e.g., Park and Levin, 2001) and *PKP* (e.g., Park and Levin, 2000) using 'receiver function'-style approaches.

1.08.3 Source Removal

With the geometric framework just described in mind, the first task in most structural studies employing teleseismic wave fields is to characterize and remove the source. The standard model is a linear convolution of the form

$$u_{in}(\mathbf{x}, t) = S(t) \otimes G_{in}(\mathbf{x}, t; \mathbf{p}_{\perp}) \qquad [1]$$

where u_{in} is the observed particle displacement/velocity in direction i at location $\mathbf{x}$ as a function of time t, $S(t)$ is an effective source time function, $\otimes$ signifies temporal convolution, and $G_{in}(\mathbf{x}, t; \mathbf{p}_{\perp})$ is a 'Green function' or, more precisely, receiver-side response to an impulsive quasi-plane-wave incident from below, which is characterized, for example, by horizontal slowness $\mathbf{p}_{\perp}$. Index n denotes the incident-wave polarization and will be omitted (or, rather, implicitly assumed) in the discussions that follow; however, it is important to acknowledge, in particular, in dealing with incident *S*-wave fields. Note that (1) is a far-field approximation that ignores finite source directivity. Early applications of receiver

functions (e.g., Langston, 1979; Phinney, 1964) implicitly approximated $S(t)$ on a teleseismic P recording by the vertical component of motion, $u_z(t)$. In the following sections, we will describe procedures whereby this approximation can be improved leading to more accurate estimates of the Green function. We begin by discussing means by which incident-wave and scattered-wave energies can be more effectively separated on different components. We will then proceed to review the minimum-phase nature of teleseismic wave fields that will allow us to simplify characterization and removal of the source. Our focus throughout this analysis will be on teleseismic P, but reference to teleseismic S will be made toward the end of the section.

1.08.3.1 Modal Decomposition

The combination of transmission geometry, precritical incidence, and modest material property gradients within the crust and upper mantle generally results in the incident-wave arrival (i.e., teleseismic P) being the most energetic feature on a seismogram windowed to exclude other principal phases, usually by at least an order of magnitude. Figure 3 demonstrates this property with synthetic seismograms for P-wave field incident upon an idealized, layer-over-a-half-space crustal model. Because the incident-wave field comprises a single-mode type that is either P or S, it is useful to decompose the observed wave field into separate modes in order to aid in source deconvolution and characterization of the scattered-wave field. In early studies, 'modal decomposition' was crudely accomplished through the identification of the vertical/radial components of displacement with dominantly P/S energy, respectively. A better isolation of energy into modes can be achieved in one of a number of ways. In principle, one could isolate P- and S-waves exactly in laterally heterogeneous, isotropic media by identifying the respective modes as the curl-free and divergence-free components of displacement. The density of recording instrumentation is rarely, if ever, sufficient, however, to accurately estimate the necessary spatial derivatives. As a practical alternative and as justified in Section 1.08.2, we may assume that the incident-wave field is dominated by a single horizontal slowness p. By further assuming that near-surface P- and S-velocities α, β are known, an approximate, 1-D, upgoing wave field separation can be used to isolate P- and S-modes (Bostock, 1998; Kennett, 1991; Reading et al., 2003), specifically,

$$\begin{pmatrix} P \\ V \\ H \end{pmatrix} = \begin{pmatrix} \dfrac{p\beta^2}{\alpha} & 0 & \dfrac{\beta^2 p^2 - 1/2}{\alpha q_\alpha} \\ \dfrac{1/2 - \beta^2 p^2}{\beta^2 q_\beta} & 0 & p\beta \\ 0 & 1/2 & 0 \end{pmatrix} \begin{pmatrix} u_r \\ u_t \\ u_z \end{pmatrix} \qquad [2]$$

where P, V, and H are estimates of the upgoing P-, SV-, and SH-component seismograms; u_r, u_t, and u_z are the radial, transverse, and vertical displacement seismograms; and q_α, q_β, and p are the vertical P, vertical S, and horizontal components of slowness at the surface, respectively. The modal field $[P,V,H]^{\mathrm{T}}$, deconvolved of source and transformed back to upgoing (Cartesian) displacement $[\hat{u}_r, \hat{u}_t, \hat{u}_z]^{\mathrm{T}}$ as

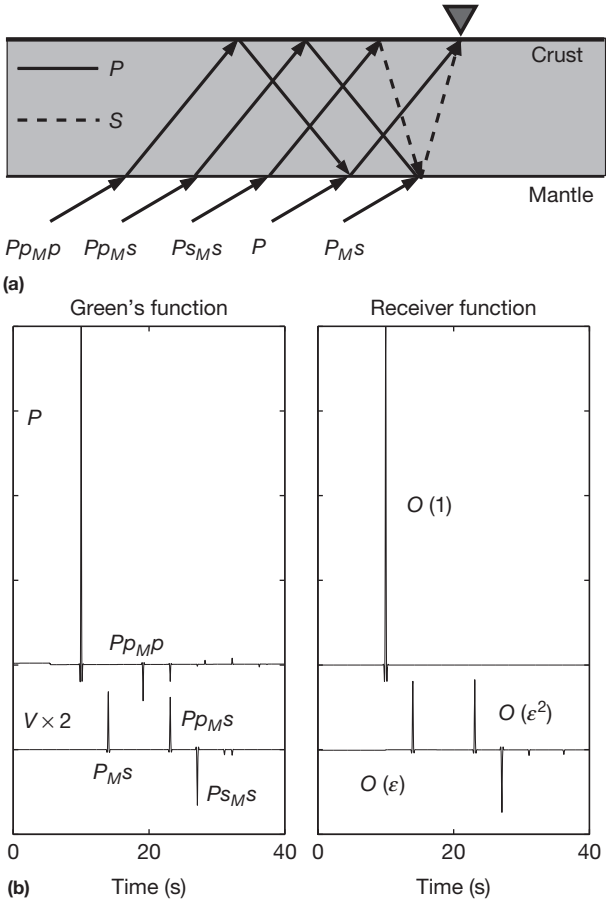

Figure 3 Synthetic seismograms for a layer-over-a-half-space, crustal model. (a) Ray paths of largest amplitude phases (P_Ms, Pp_Mp, Pp_Ms, and Ps_Ms) scattered crustal phases from the crust–mantle boundary resulting from an incident P-wave field (P-wave legs, solid; S-wave legs, dashed). See Figure 4 for examples of these phases on observed seismograms. (b) Left panel shows the Green function P and (SV) seismograms with phases labeled, and right panel comprises the corresponding time series in the receiver function approximation. Note that the direct P arrival dominates the Green function and that the receiver function is a leading-order approximation to the Green function correct to $O(1)$ on the P-component and to $O(\varepsilon)$ on the SV-component where $\varepsilon \ll 1$ measures the amplitude of the first-order scattered field relative to the incident wave.

$$\begin{pmatrix} \hat{u}_r \\ \hat{u}_t \\ \hat{u}_z \end{pmatrix} = \begin{pmatrix} \alpha p & \beta q_\beta & 0 \\ 0 & 0 & 1 \\ \alpha q_\alpha & -\beta p & 0 \end{pmatrix} \begin{pmatrix} P \\ V \\ H \end{pmatrix} \qquad [3]$$

(vs. the original displacement field $[u_r, u_t, u_z]^{\mathrm{T}}$ that contains both upgoing and downgoing waves), is generally the quantity that will be required in the inverse-scattering analysis of subsequent sections. Note that the near-surface velocities α, β can be determined from the data (assuming known slowness) from measurements of first-motion amplitudes on seismograms representing individual, incident P- and S-waves (Bostock and Rondenay, 1999; Helmberger, 1968) or, equivalently, from the zero-lag amplitudes of radial/vertical receiver functions (Ammon, 1991).

This approach can be generalized to the treatment of ocean-bottom recordings where the reverberatory effect of the ocean column is to be mitigated. Isolation of the upgoing wave field at the top of the solid medium (i.e., oceanic crust) is once more desirable since the ocean column reverberations are downgoing at this location. Several formulations are possible within a 1-D context. If pressure gauge recordings are available in addition to ocean-bottom displacement, then the decomposition can be accomplished along with the knowledge of material properties at the ocean bottom (e.g., Amundsen and Reitan, 1995; Thorwart and Dahm, 2005). Alternatively, if water depth is known together with ocean-bottom displacement and material properties, then recovery of the upgoing wave field is also possible (Bostock and Tréhu, 2012).

An alternative approach to modal decomposition for land observations involves rotation of the particle displacement field to a coordinate system where maximum energy is transferred to a single component. The angle of rotation can be determined by diagonalizing the displacement covariance matrix C (Vinnik, 1977) defined as

$$\mathrm{C} = \begin{pmatrix} \int_{t_1}^{t_2} \mathrm{d}t\, u_r^2(t) & \int_{t_1}^{t_2} \mathrm{d}t\, u_r(t) u_z(t) \\ \int_{t_1}^{t_2} \mathrm{d}t\, u_r(t) u_z(t) & \int_{t_1}^{t_2} \mathrm{d}t\, u_z^2(t) \end{pmatrix} \qquad [4]$$

where $[t_1, t_2]$ is a time window that encompasses the energy associated with the primary phase. The latter approach fails to acknowledge the presence of the free surface (and, more specifically, the generation of downgoing waves therefrom) but may be used where the incident slowness is unknown or the wave field is distorted by strong, laterally heterogeneous structure. A more detailed comparison of the two approaches is made by Svenningsen and Jacobsen (2004).

1.08.3.2 Receiver Functions and the Property of Minimum Phase

Once modal decomposition has been accomplished, we shall (either implicitly or explicitly) draw upon an important property of teleseismic body-wave fields to remove the effects of the source, namely, that the underlying Green function component in the incident mode (i.e., the *P*-component of teleseismic *P*) is minimum phase. To provide intuitive justification for the minimum-phase assertion, we consider the seismograms in Figure 3(b) and note that the incident *P*-wave at $t=0$ clearly dominates other arrivals in amplitude. In particular, let us normalize the amplitude of this arrival to unity, such that the amplitudes of the first-order scattered phases (i.e., those phases that have reflected/converted once from heterogeneity, not including the free surface) are of order ε. Because material property contrasts are small and scattering interactions occur at near-normal incidence, we have in general that $\varepsilon \ll 1$. Multiply scattered-wave fields (i.e., two or more reflection/conversion interactions with subsurface heterogeneity) attenuate as ε^n where n is the order of scattering and can be safely neglected in most applications. Accordingly, we may characterize the modal component of the Green function in the incident mode as, for example, $G^P(t) \sim \delta(t) + s(t)$, where $\delta(t)$ is the delta-function direct arrival and $s(t)$ represents the scattered field and is $O(\varepsilon)$ in amplitude. Following Claerbout (1976), we shall examine the properties of the $G^P(t)$ in the frequency domain, that is, $G^P(\omega)$. As shown in Figure 4, the delta-function makes a purely real contribution to the spectrum that is constant, say, 1, for all frequencies. Moreover, if the amplitude spectrum of $s(t)$, that is, $s(\omega)$, is <1 for all frequencies, we note that it is impossible for the phase of $G^P(\omega) = 1 + s(\omega)$ to wrap around the origin. This scenario thus constitutes a sufficient condition for $G^P(t)$ to be minimum phase. If a signal is minimum phase, it is by definition that signal, among all signals sharing the same amplitude spectrum, which possesses maximum possible energy concentrated near its onset (Robinson and Treitel, 1980). Bostock (2004) provided a more detailed justification and examination of the conditions under which the minimum-phase assumption is likely to apply to teleseismic wave fields (see also, Li and Nabelek, 1999; Sherwood and Trorey, 1965). We note at this juncture that an effective modal decomposition, as outlined in the previous section, is important in this regard as it improves the likelihood that the estimated *P*-component impulse response is minimum phase by ensuring that the delta-function $\delta(t)$ in the definition of $G^P(t)$ is of maximum possible amplitude relative to the scattered waves $s(t)$.

The minimum-phase property is important in at least two respects. First, it implies that energy is strongly concentrated at early times within the time series. In particular, the *P*-component, teleseismic *P* Green function is to leading

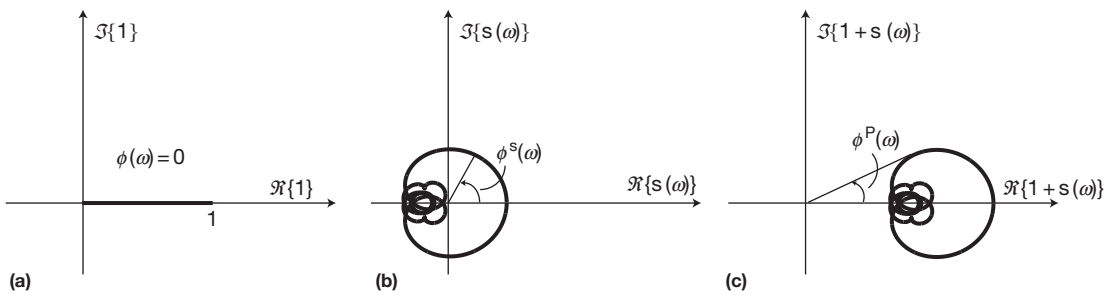

Figure 4 Frequency-domain description of $G^P(t) = \delta(t) + s(t)$. (a) Direct wave. The direct wave is represented by a delta-function at time 0 and is thus pure real, constant (amplitude 1) with phase $\phi(\omega) = 0$ for all frequencies ω. (b) Scattered waves. The scattered-wave spectrum $s(\omega)$ is characterized by an amplitude spectrum $|s(\omega)| < 1$ and a more general phase spectrum $\phi^s(\omega)$. (c) $G^P(\omega)$. The total spectrum is characterized by a real component that is positive for all ω, thereby ensuring that $G_P(t)$ is minimum phase. Reproduced from Claerbout JF (1976) *Fundamentals of Geophysical Data Processing*. New York, NY: McGraw-Hill.

order $O(1)$ a delta-function. Consequently, an observed P-component seismogram can be taken to be an estimate of the earthquake source time function that is accurate to leading order. Moreover, deconvolution of the corresponding S-component with the P-component will result in an estimate of the S-component Green function that is correct to leading order, that is, $O(\varepsilon)$, since the S-component of teleseismic P comprises only scattered (converted) waves. The foregoing argument provides justification for the validity of the classic receiver function as a leading-order estimate of the S-component of the teleseismic P Green function. Indeed, interpretation of the receiver function as a series of discrete, scattered arrivals from subsurface discontinuities relies intrinsically on this observation. In situations where the minimum-phase assumption is questionable, for example, at regional distances where several incident arrivals with comparable magnitudes and different slownesses originate from triplication at transition zone discontinuities (cf. Park and Levin, 2001), interpretation must proceed with caution. In such cases, the receiver function (i.e., spectral ratio of different modal components) can no longer be considered as good an approximation to the Green function, although it may still possess utility as a source-independent transfer function.

A second point of importance is that the minimum-phase property affords insight into how more accurate estimates of the Earth's true Green function can be recovered. Improved knowledge of the P-component Green function is particularly desirable because this component is a simple delta-function (i.e., the direct wave) within the receiver function approximation. That is, it contains no information on pure P (i.e., P-to-P) scattering whatsoever. The P-to-P scattering mode is important because its amplitude provides constraints on short-wavelength variations in subsurface compressional moduli (e.g., P-impedance, P-velocity, and bulk modulus). Amplitudes of conversions and pure S reflections, in contrast, have first-order sensitivity only to shear properties (e.g., S-impedance and S-velocity) (see, e.g., Aki and Richards, 2002). Numerous authors (e.g., Bostock and Rondenay, 1999; Bostock and Sacchi, 1997; Clayton and Wiggins, 1976; Langston and Hammer, 2001; Li and Nabelek, 1999; Paulssen et al, 1993; Revenaugh, 1995; Zhu and Kanamori, 2000) have exploited the minimum-phase property within a multichannel context to procure better estimates of the teleseismic P Green function. In these studies, P-component time series from a number of stations recording the same earthquake are time-normalized and averaged in some fashion to approximate the source. Weaker ($O(\varepsilon)$ in amplitude) scattered-wave contributions at different stations are assumed to be incoherent in time and thus sum destructively, whereas the incident wave, $O(1)$ in amplitude and fixed at time 0 on all traces, adds constructively to produce a scaled estimate of the true source time function. The teleseismic P Green function is then recovered by deconvolving this source estimate from both P- and S-component seismograms recorded at all stations. The main drawback to this approach is that the signal from structure that exhibits little or no lateral variation (e.g., the continental Moho in many instances) is identified with the source and, consequently, is not represented in the deconvolved Green function estimates. We shall describe an alternative to this approach in the succeeding text that also relies on the minimum-phase property but does not suffer from this last shortcoming.

1.08.3.3 Improved Teleseismic *P* Green Functions

The minimum-phase property implies that knowledge of the P-component amplitude spectrum alone is sufficient to define the time-domain function, since its phase, ϕ^P, is simply related to amplitude A^P through

$$\phi^P(\omega) = \mathcal{H}\{\log(A^P)\} \qquad [5]$$

where $\mathcal{H}\{\ \}$ denotes Hilbert transform (e.g., Claerbout, 1976). In fact, the phase of all three components of motion (or, more specifically, upgoing P, SV, and SH), as well as the source, need not be considered until their respective amplitude spectra have been recovered. As explained by Baig et al. (2005) and Mercier et al. (2006), estimation of, for example, the source amplitude spectrum can be accomplished by considering the cross spectrum of two seismograms sharing that source. As an example, consider two components P and SV of the same three-component recording represented in the frequency domain as $P(\omega)$, $V(\omega)$. Their cross spectrum can be written as

$$P(\omega)V^*(\omega) = |S(\omega)|^2 |G^P(\omega)||G^V(\omega)| e^{i(\phi^P - \phi^V)} \qquad [6]$$

where $|G^P(\omega)|$, $|G^V(\omega)|$, and $|S(\omega)|$ are amplitude spectra of the Green function components and the source, respectively, and * denotes complex conjugate. Note that the source enters the cross spectrum as a common convolutional element and that, accordingly, it does not contribute to the cross spectrum phase, $\phi^P - \phi^V$. We can say, therefore, that the source makes a zero-phase contribution to the cross spectrum $P(\omega)V^*(\omega)$. There are several algorithms that can, in principle, be utilized to isolate the zero-phase component of a signal (Hayes et al., 1980) and thus to form an estimate of $|S(\omega)|$ under the assumption that the cross spectrum of the two Green function components, that is, $G^P(\omega)GV^*(\omega)$, contains no zero-phase component. Moreover, by appealing to causality and a propagation model that includes a dominantly 1-D lower mantle, the duration of the two components $P(t)$ and $V(t)$ in the time domain will determine the maximum depth to which scattered energy is mapped to the Green function cross spectrum. All scattered signals generated in advance of this depth will either arrive outside the recording interval (in the case of conversions) or be mapped to $|S(\omega)|$ (in the case of same mode interactions). The latter result is a beneficial consequence for studies of receiver-side structure.

The procedures for zero-phase signal extraction tend, unfortunately, to be highly sensitive to noise, and Baig et al. (2005) discussed modifications based on spectral smoothing that tend to improve recovery on synthetic examples. Nonetheless, it is advantageous, when possible, to further improve upon estimates by making use of multichannel measurements. Even a single, three-component seismogram will afford three independent estimates of a common source, and when multiple stations and events are available, this number can increase dramatically. Consider, for example, a data set comprising J stations recording I three-component seismograms. By casting the convolution relation in the log-spectral domain such that a single recording representing source i and impulse response j is represented as, for example,

$$\log(|P_{ij}(\omega)|) = \log(|S_i(\omega)|) + \left(\left|G_j^P(\omega)\right|\right) \qquad [7]$$

we may generate a large linear system of equations (see Andrews, 1986) that includes $3IJ$ equations in $I + 3J$ unknowns.

This system, when augmented with equations that include source estimates $|S_i(\omega)| \approx |\widetilde{S}_i(\omega)|$ determined as outlined in the preceding text, becomes highly redundant and can be solved via least squares to recover the improved amplitude spectra $|G_j^P(\omega)|$, $|G_j^V(\omega)|$, $|G_j^H(\omega)|$, and $|S_i(\omega)|$. The phase of $G_j^P(\omega)$ is readily determined directly through eqn [5], whereas the phase of the two remaining quantities can be recovered through a slightly more involved procedure described by Mercier et al. (2006). An example showing the teleseismic *P* Green function estimates as a function of horizontal slowness for station HYB at Hyderabad, India, is shown in Figure 5. The *P*-image clearly reveals the pure *P* surface–Moho reflection that cannot be recovered through conventional receiver function analysis.

The approach outlined in this section can in principle be applied to *P* phases other than teleseismic *P* (e.g., *PP* and *PKP*) provided that these recordings are free of other primary phases. We consider its relevance and application to *S* phases in the succeeding text.

1.08.3.4 The Teleseismic *S* Green Functions

There are two principal complications that arise when seeking to extend the approach of the previous section to *S* phases, both of which concern the applicability of the minimum-phase assumption. The first complication is primarily theoretical in nature and is easily qualified. The second issue pertains to the polarization of *S*-waves and poses more practical difficulty. We discuss each in turn.

We have already alluded to the increased tendency for multiply interfering phases (e.g., teleseismic *S*, *ScS*, and *SKS*) within the teleseismic *S*-wave field in some circumstances but will assume that these complications have been dealt with and that our observations represent a single, direct phase with known slowness. Strictly speaking, the *S*-component of the impulse response (i.e., the *S*-component of the teleseismic *S* Green function) cannot be minimum phase in the presence of heterogeneity owing to the generation of acausal, for example, *S*-to-*P*-to-*S* scattering interactions that arrive as *S*-waves in advance of the incident *S*-wave field. These early arrivals are, however, of order $O(\varepsilon^2)$ in amplitude and so can be ignored within the single-scattering formulations that dominate inversion practice (see Sections 1.08.4 and 1.08.5).

The next issue, then, is to determine to which component of *S* the minimum-phase assumption should apply. In 1-D, isotropic (or transversely isotropic) media, this question is easily addressed since *P*/*SV* and *SH* interactions are decoupled and the minimum-phase assumption can be made independently for both the *SV*- and *SH*-components of motion. A number of earlier studies (Båth and Stefánson, 1966; Baumgardt and Alexander, 1984; Bock, 1991; Faber and Müller, 1980; Jordan and Frazer, 1975; Sacks et al., 1979) have avoided source deconvolution by employing deep focus events to examine *SV*-to-*P* conversions. More recently, the teleseismic *SV* Green/receiver functions have been generated in a manner directly analogous to teleseismic *P* by simply interchanging the roles of the *P*- and *SV*-components (e.g., Kumar et al., 2005; Li et al., 2004; Vinnik et al., 2005) or by using teleseismic *P* as a source estimate (Zhou et al., 2000). Considerably less attention has been paid to *SH* due to the lack of conversions in isotropic, 1-D media, although multichannel stacking has been used in at least one study to recover *SH* reflections from dipping structures (Li, 1996).

In more realistic circumstances, particularly those involving azimuthal anisotropy, we recognize, however, that *S*-waves with different polarizations will couple such that the impulse response becomes a more complex function of the incident *S*-polarization (Farra et al., 1991). Our objective in this class of study is thus to extract an azimuth-dependent and polarization-dependent impulse response (Farra and Vinnik, 2000; Frederiksen and Bostock, 2000). Because (quasi-)*S*-modes propagate at different velocities in anisotropic media, situations will

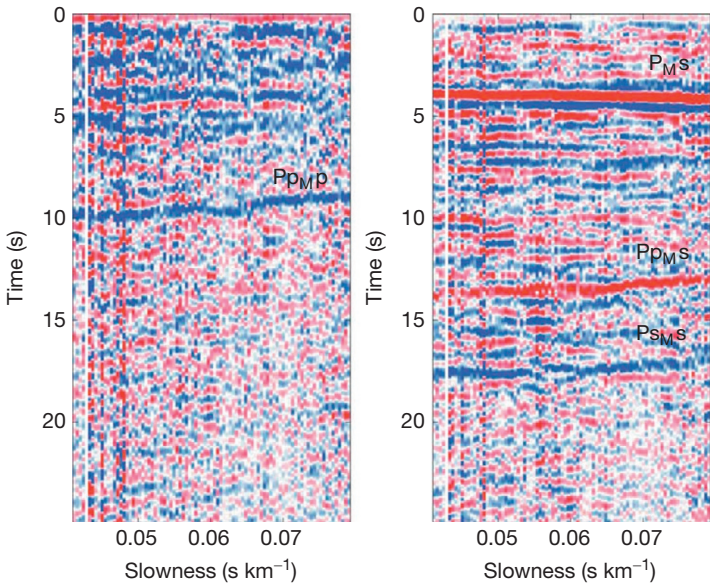

Figure 5 The teleseismic *P* and *SV* Green function estimates for station HYB, India, as function of horizontal slowness $\sqrt{p_\alpha p_\alpha}$ (reproduced from Kumar MR and Bostock MG (2006) Transmission to reflection transformation of teleseismic wavefields. *Journal of Geophysical Research* 111: B08306). Note the clear definition of the main first-order scattered phases from the continental Moho on both components, as defined in Figure 3.

frequently arise where at least one component of S-motion recorded at the surface is decidedly non-minimum phase.

To address this issue, we write the upgoing wave field (which contains both direct- and scattered-wave contributions) recorded at the surface $[P, V, H]^{\mathrm{T}}$ in terms of a purely S-wave field $[0, V_0, H_0]^{\mathrm{T}}$ incident at the base of laterally homogeneous, generally anisotropic, receiver-side stratification,

$$\begin{pmatrix} P \\ V \\ H \end{pmatrix} = \begin{pmatrix} U^{PP} & U^{PV} & U^{PH} \\ U^{VP} & U^{VV} & U^{VH} \\ U^{HP} & U^{HV} & U^{HH} \end{pmatrix} \begin{pmatrix} 0 \\ V_0 \\ H_0 \end{pmatrix} \qquad [8]$$

where the various elements of the transmission matrix for upgoing waves $\mathrm{U} = \mathrm{U}(\omega, \mathbf{p}_{\perp})$ are functions of frequency and horizontal slowness p_α, $\alpha = 1, 2$. Note that the matrix U can be related to the transmission matrix T_U for upward incidence in the absence of a free surface as $\mathsf{U} = \left(\mathsf{I} - \mathsf{R}_D \widetilde{\mathsf{R}}\right)^{-1} \mathsf{T}_U$ (Kennett, 1983) where the effects of reverberation are expressed through the free-surface reflection matrix $\widetilde{\mathsf{R}}$ and reflection matrix R_D for the stratification in the absence of free surface. We will further assume that the incident-wave field $[0, V_0, H_0]^{\mathrm{T}}$ is linearly polarized as would be the case for a simple, for example, double-couple, point source within an isotropic source-side structure. Upon arrival at the surface, the V,H-components can combine to produce an elliptically polarized wave field characterized by low eccentricity that is the manifestation of shear-wave splitting (e.g., Silver and Chan, 1991; Vinnik et al., 1989). This observation indicates that the elements U^{HV} and U^{VH} can be comparable in magnitude to the diagonal elements of U for structures representing the real Earth.

An obvious way to proceed is thus to follow standard practice for shear-wave splitting analysis and search for the combination of fast-polarization direction and delay time that most nearly corrects for shear-wave splitting to produce a linearly polarized estimate of V_0 and H_0. Although this downward continuation (i.e., simulation of U^{-1}) is only approximate in that internal reverberations/reflections are neglected, our main concern is with the dominant, incident S-arrival. In particular, the component of the resulting time series in the polarization direction, say, $\mathbf{s}_0$, will then be minimum phase under the condition that the incident wave has been reduced to a single impulse on one component and is more energetic than all remaining signals. Accordingly, the source can be removed following the approach taken in **Section 1.08.3.3** for P-waves. Once the source is removed, we may reverse the downward continuation (including errors therein) by applying the forward-splitting operator to produce the corresponding source-deconvolved surface wave field $[P, V, H]^{\mathrm{T}}$. To create the Green function, it remains to distinguish between the impulse responses produced by individual V_0 and H_0. We may exploit multichannel measurements taken at the same horizontal slowness $p_\alpha = [p_1, p_2]$ (i.e., seismograms representing different source mechanisms but the same geographical source–receiver combinations) to this end, by taking appropriate linear combinations of the deconvolved $[P, V, H]^{\mathrm{T}}$ as dictated by independent values of $\mathbf{s}_0$.

The approach outlined in the preceding text may break down where source-side anisotropy has contributed to splitting or where a single fast-polarization direction and delay time do not adequately characterize the transmission response. This latter situation may arise where multiple, strongly anisotropic layers exist. In these cases, a single measured $\mathbf{s}_0$ may not accurately represent the polarization state of the wave field incident on receiver-side heterogeneity (e.g., Silver and Savage, 1994). Farra and Vinnik (2000) described an alternate procedure, also using multichannel measurements, for computing the S-receiver function by deconvolving the P-component with the projection of the S-wave in the direction of the strongest polarization. The interpretation of this quantity faces the same restrictions identified in the preceding text and is based on a linearization, which limits allowable relative magnitudes of off-diagonal elements in U.

1.08.3.5 Deconvolution, Stacking, and Array Processing

Our focus throughout the majority of this section has been to establish the physical basis for the classical receiver function and extensions that allow us to recover a more fundamental quantity, namely, the Green function, which is required in the inverse-scattering approaches to be described in **Sections 1.08.4.3** and **1.08.5**. In so doing, we have paid little attention to a significant body of work that has been devoted to a more general topic of signal processing as applied to teleseismic wave fields, specifically deconvolution. In the main, this work is concerned with estimating a transfer function (i.e., either receiver function or the Green function) such that the effect of noise is mitigated, usually under the assumption that the source wavelet is perfectly known. We provide, in the succeeding text, a brief overview of deconvolution applications to receiver-side scattering of teleseismic wave fields.

Among the first attempts to extract an impulse response from teleseismic body waves, Ulrych and coworkers (Ulrych, 1971; Ulrych et al., 1972) employed filtering in the cepstral domain to separate source from structural signal. The cepstrum of a signal is computed by inverse Fourier transformation of the logarithm of its Fourier transform. That and eqn [7] are therefore termed homomorphic decompositions since they transform the convolutional operation to an additive one (see, e.g., Oppenheim and Schafer, 1975). The difficulty in applying such homomorphic decompositions to non-zero-phase signals (vs. autocorrelations) resides in the necessity for phase unwrapping, which effectively renders the approach intractable for many practical purposes. This shortcoming was noted by Clayton and Wiggins (1976) who proposed an alternative 'water-level' method that has subsequently found widespread use. The receiver function $R(t)$ is thereby computed as

$$R(t) = \mathcal{F}^{-1}\left\{\frac{P^*(\omega)S(\omega)}{\max\left(P^*(\omega)P(\omega), cP_{\max}{}^*P_{\max}\right)}\right\} \qquad [9]$$

where $\mathcal{F}^{-1}\{\}$ denotes inverse Fourier transformation, $P_{\max}$ is the spectral value for which $P(\omega)$ achieves maximum absolute value, and c is a user-specified water-level parameter that regularizes the deconvolution by damping contributions at frequencies where signal levels are low and thus more likely to be corrupted by noise. Note that when $c = 0$, eqn [9] reduces to simple spectral division, whereas large values of c produce a receiver function that is a scaled cross correlation of the P- and S-components. In the latter case, the P-component acts as a matched filter (Kind and Vinnik, 1988). Variations on this

same theme include the standard damped least-squares deconvolution solution

$$R(t) = \mathcal{F}^{-1}\left\{\frac{P^*(\omega)S(\omega)}{P^*(\omega)P(\omega)+\delta}\right\} \quad [10]$$

where δ is a constant Tichonov regularization parameter determined by standard (e.g., L-curve, generalized cross validation (Golub et al., 1979)) means and Wiener deconvolution (e.g., Press et al., 1986) where δ in eqn [10] becomes frequency-dependent and proportional to the pre-event noise spectrum. When multichannel measurements representing the same $R(t)$ are available, it is advisable to compute a simultaneous estimate (Gurrola et al., 1995) as

$$R(t) = \mathcal{F}^{-1}\left\{\frac{\sum_i P_i^*(\omega)S_i(\omega)}{\sum_i P_i^*(\omega)P_i(\omega)+\delta}\right\} \quad [11]$$

rather than stacking individual estimates computed by, for example, eqn [10] because only one value of δ needs to be chosen and that value is likely to be small since different seismograms will, in general, exhibit spectra with different signal-to-noise characteristics. Park and Levin (2000) advocated using multitaper spectral estimates (Thomson, 1982) to help stabilize receiver function deconvolution, where the individual multichannel recordings within the sums in eqn [11] are replaced by the tapered spectral estimates for a single seismogram.

While quadratic misfit and model norms are being considered, Parseval's theorem ensures that the results of deconvolution in the time domain and frequency domain will be equivalent, and it is therefore expedient to perform computations in the frequency domain to take advantage of the fast Fourier transform. Time-domain deconvolution may be desirable, however, where time-domain-specific regularization of $R(t)$ such as sparseness is required (Gurrola et al., 1995; Ligorria and Ammon, 1999).

In addition to deconvolution, nonlinear stacking and array processing methods are often used to improve signal-to-noise levels on teleseismic body-wave recordings and, in particular, for emphasizing discrete, weak arrivals. Popular nonlinear stacking techniques include the Nth root stack (Muirhead and Datt, 1976) and the phase-weighted stack (Schimmel and Paulssen, 1997); Kennett (2000) discussed the application of these approaches to multicomponent teleseismic wave fields. In the next two sections, we will examine multichannel processing of scattered teleseismic wave fields in the context of structural inversion for which (weighted but linear) stacking enters naturally through surface integration. For a summary of more general array processing techniques applied to teleseismic wave fields, the reader is referred to Rost and Thomas (2002).

1.08.4 1-D Inversion

The use of single-station data in early receiver function studies forced practitioners to focus attention on delineation of strictly 1-D structures. In fact, this practice is still commonplace today because, in many circumstances, the target discontinuities are expected to be locally horizontal or to vary slowly in lateral coordinates. Thus, for example, in studies of the continental crust (e.g., Owens et al., 1984; Zandt and Ammon, 1995) and transition zone discontinuities (e.g., Chevrot et al., 1999; Kind and Vinnik, 1988; Vinnik, 1977), the 1-D analysis has proved to be quite adequate and has yielded valuable information on the characteristics of these structures in different tectonic regimes. The more recent documentation of near-horizontal, anisotropic discontinuities within the continental lithosphere (Asencio et al., 2003; Bostock, 1997, 1998; Leidig and Zandt, 2003; Levin and Park, 1997, 1998; Saul et al., 2000) has opened new avenues for study with regard to both inverse modeling and complementary new information that anisotropy can potentially deliver on subsurface structures and dynamics.

Methods employed to invert receiver functions for 1-D variations in material properties can be classified into three categories: optimization based on least squares, Monte Carlo methods, and inverse scattering. We discuss each category in turn but pay special attention to the last method because it is most closely tied to the physics of scattering and provides formal justification for the 'delay-and-sum' and 'squeezing and stretching' approaches that have dominated 1-D studies of lithospheric and upper mantle discontinuities to date.

1.08.4.1 Least-Squares Optimization

Optimization by least squares is the most widely used and generic method for solving geophysical inverse problems (Menke, 1984; Parker, 1994). It is less expensive than Monte Carlo inversion and, in the context of teleseismic body waveforms, makes less stringent demands on data than inverse-scattering methods. More specifically to the latter point, data insufficiency (in the form, say, of limited frequency and/or slowness content) can be readily compensated for through model regularization, and there is no formal requirement that data be supplied in the form of the Green functions. That is, model matching by least-squares techniques can be directly undertaken using transfer functions, for example, the receiver function, without concern for the proximity of this quantity to the true Green function. All that is required is a means of performing receiver function forward modeling.

Implementation is straightforward (see, e.g., Ammon et al. (1990) for a more detailed account). A receiver function or series of receiver functions strung end to end and represented in either the time or frequency domain is assembled within a vector d, with individual elements d_i. For consistency with later notation, we shall define c to be a vector containing the elasticities and densities of a sequence of horizontal layers bounded by a free surface above and half-space below, thereby representing a 1-D Earth model. The forward-modeling operator is represented by a (nonlinear) functional $\mathcal{D}$ that operates on c to produce synthetic data, that is,

$$\mathsf{d} = \mathcal{D}\{\mathsf{c}\} \quad [12]$$

In the 1-D context, both exact layer-matrix methods (Ammon et al., 1990; Haskell, 1962; Kennett, 1983; Kind et al., 1995; Kosarev et al., 1993) and approximate ray methods (e.g., Langston, 1977; Owens et al., 1984) are feasible means of representing $\mathcal{D}$. Ray methods are more economical in time-domain implementations where only a limited number of low-order scattering interactions are to be modeled, whereas layer-matrix methods provide a complete representation wherein economies

may be gained by restricting computation to the range of frequencies and slowness that characterize the data.

Nonlinearity is addressed in the inverse problem by expanding the receiver function vector as a Taylor series about a starting model c_0, such that

$$d_i = \mathcal{D}_i(\mathsf{c}) = \mathcal{D}_i\{\mathsf{c}_0\} + \frac{\partial \mathcal{D}_i}{\partial c_j}\{\mathsf{c}_0\}\Delta c_j + O\left(||\Delta \mathsf{c}||^2\right) \qquad [13]$$

Rearranging eqn [13], discarding nonlinear terms, and writing in matrix form yield

$$\mathsf{W}\Delta\mathsf{c} = \mathsf{f} \qquad [14]$$

where the data residual vector is $\mathsf{f} = \mathsf{d} - \mathcal{D}(\mathsf{c}_0)$ and the elements of the sensitivity matrix W are defined by $W_{ij} = \partial\mathcal{D}_i/\partial c_j$. Randall (1989) described a particularly economical means to compute W_{ij} for receiver function inversions that exploits Kennett's (1983) reflection/transmission layer-matrix formalism. Alternatively, this quantity can be determined numerically. Since receiver functions are sensitive primarily to short-wavelength structure, c_0 is generally taken to represent a slowly varying velocity model on which the unknown short-wavelength perturbation Δc is superposed.

The solution of the linear system [14] can be accomplished in a number of ways, although minimization of the quadratic norm of f leading to solution of the normal equations is the standard approach. Depending on the form of model parameterization (e.g., layer thicknesses), the system in eqn [14] may be rank-deficient in which case regularization via, for example, damping can be implemented. Further accommodation of nonlinearity can, in principle, be accomplished by Newton iteration on eqn [13].

1.08.4.2 Monte Carlo Inversion

The advent of high-performance computing and the relatively few model parameters that characterize 1-D problems have led to investigation of Monte Carlo methods for performing receiver function inversions. These methods require only a forward-modeling engine without need for calculation of derivatives (i.e., W_{ij}), since the sole criterion for model selection is an arbitrary measure of fit. They hold the distinct advantage over least-squares optimization that they are global in nature and less apt to identify incorrect, local misfit minima as solutions. Although the number of unknowns is relatively small, a purely random sampling of the model space is still computationally demanding and, at best, inefficient. Consequently, preference has been given to 'directed search' algorithms that exploit information from past computations to guide future sampling. Two examples of directed search algorithms that have been applied to receiver function inversion are the genetic algorithm (Clitheroe et al., 2000; Goldberg, 1989; Lawrence and Wiens, 2004; Shibutani et al., 1996) and the recently introduced nearest-neighbor algorithm (Frederiksen et al., 2004; Lucente et al., 2005; Nicholson et al., 2005; Sambridge, 1999a). Both algorithms begin with a population of models generated through an initial (uniform or random) sampling of model space. Genetic algorithms employ an evolutionary analogy wherein model parameters are encoded within binary strings or 'chromosomes.' The model population is allowed to evolve through iterations (or 'generations') by stochastic selection of models based on goodness of fit, by recombination of models (through chromosomal splicing), and by random 'mutation.' The natural neighborhood algorithm employs an adaptive Voronoi cellular network to drive the parameter search, where each successive iteration randomly samples the model space within cells occupied by the fittest models of the previous iteration. The algorithm thereby focuses increasingly on regions in model space that produce models that come closer to satisfying the data. Another important advantage of these directed search approaches lies in the output of model populations that afford the opportunity for either qualitative or quantitative (Sambridge, 1999b) appraisal of the model space.

1.08.4.3 Born Inversion and Classic (Delay and Sum) Studies

Unlike the two methods just described, inverse-scattering approaches to the receiver function inversion problem rely fundamentally on an explicit description of the scattering process. Accordingly, the starting point is the Lippman–Schwinger equation that we shall write in the frequency domain as (see Hudson and Heritage, 1981)

$$\Delta u_n(\mathbf{x}',\omega) = \int_V \mathrm{d}\mathbf{x}\left(-\Delta c_{ijkl}(\mathbf{x})\partial_k u_l(\mathbf{x},\omega)\partial_j G^0_{in}(\mathbf{x},\mathbf{x}',\omega) + \Delta\rho(\mathbf{x})\omega^2 u_i(\mathbf{x},\omega)G^0_{in}(\mathbf{x},\mathbf{x}',\omega)\right) \qquad [15]$$

This equation is cast in terms of field quantities and perturbations in material properties whose support is the volume V. The material properties of the medium are described by the stiffness tensor c_{ijkl} and density ρ through

$$c_{ijkl}(\mathbf{x}) = c^0_{ijkl}(\mathbf{x}) + \Delta c_{ijkl}(\mathbf{x}), \quad \rho(\mathbf{x}) = \rho^0(\mathbf{x}) + \Delta\rho(\mathbf{x}) \qquad [16]$$

where quantities with superscript '0' denote those of a background reference medium and the 'Δ' quantities are perturbations. Although not strictly required at this stage, we shall assume that short-wavelength heterogeneity is represented within $\Delta c_{ijkl}(\mathbf{x})$, $\Delta\rho(\mathbf{x})$ and ascribe the smoothly varying component of the material property perturbations to $c^0_{ijkl}(\mathbf{x})$, $\rho^0(\mathbf{x})$. The total wave field u_i is defined as

$$u_i(\mathbf{x},\omega) = u^0_i(\mathbf{x},\omega) + \Delta u_i(\mathbf{x},\omega) \qquad [17]$$

where $u^0_i(\mathbf{x},\omega)$ is the incident (or 'reference') wave field, created by a source with $\delta(t)$ time dependence, that would propagate independently in a medium with properties $c^0_{ijkl}(\mathbf{x})$, $\rho^0(\mathbf{x})$. Note that this definition is consistent with our earlier designation of the incident-wave field as a primary phase such as teleseismic P or S propagating through a smoothly varying mantle. The scattered (or 'perturbed') wave field $\Delta u_i(\mathbf{x},\omega)$ arises through the interaction of $u^0_i(\mathbf{x},\omega)$ with short-wavelength structure $\Delta c_{ijkl}(\mathbf{x})$, $\Delta\rho(\mathbf{x})$. We will assume that an accurate representation of $\Delta u_i(\mathbf{x}',\omega)$ has been secured using methods described in **Section 1.08.3** where $\mathbf{x}' = [x'_1, x'_2, 0]^{\mathrm{T}}$ shall be taken in this and the following sections to parameterize the Earth's surface. The quantity $G^0_{in}(\mathbf{x},\mathbf{x}',\omega)$ represents the Green function for the reference medium and will be determined analytically. We now make the customary 'single-scattering' or 'Born' approximation by assuming that $\Delta u_i(\mathbf{x})$ is small relative to $u^0_i(\mathbf{x},\omega)$ such that we may rewrite eqn [15] as

$$\Delta u_n(\mathbf{x}',\omega) \approx \int_V \mathrm{d}\mathbf{x}\left(-\Delta c_{ijkl}(\mathbf{x})\partial_k u_l^0(\mathbf{x},\omega)\partial_j G_{in}^0(\mathbf{x},\mathbf{x}',\omega) + \Delta\rho(\mathbf{x})\omega^2 u_i^0(\mathbf{x},\omega)G_{in}^0(\mathbf{x},\mathbf{x}',\omega)\right) \quad [18]$$

(see Chapter 1.05 for an account of the Born approximation in an acoustic context). Note that this step is analogous to the linearization of eqn [13] where the forward-modeling operator (or, more specifically, $\mathcal{D}_i\{\mathsf{c}\} - \mathcal{D}_i(\{\mathsf{c}_0\})$) is given by eqn [15].

To set the problem in a form that is appropriate for plane-wave propagation in a 1-D Earth, we recognize that plane waves (or, more precisely, wave fields with constant horizontal slowness p_α, $\alpha = 1, 2$) propagate independently in media exhibiting strictly vertical variations in material properties, that is, $\Delta c_{ijkl}(x_3)$, $\Delta\rho(x_3)$. Since propagation takes place in the reference medium, we will make use of plane-wave, modal expansions for $u^0(\mathbf{x}, \omega)$ and $G_{in}^0(\mathbf{x},\mathbf{x}',\omega)$ that also employ the high-frequency or WKBJ approximation. Following Bostock (2003) (and correcting an error in eqn [32] therein), we write

$$u_i^0(\mathbf{x},\omega) = \sum_r A^r(x_3)s_i^r(x_3)\mathrm{e}^{\mathrm{i}\omega(\tau^r(x_3)+p_\alpha x_\alpha)} \quad [19]$$

$$G_{in}^0(\mathbf{x},\mathbf{x}',\omega) = \sum_s \frac{-\mathrm{i}s_n^s(0)s_i^s(x_3)\mathrm{e}^{\mathrm{i}\omega\left(\tau^s(x_3,0)+p_\alpha\left(x'_\alpha - x_\alpha\right)\right)}}{2\omega\sqrt{\rho^0(0)\rho^0(x_3)\left|U_3^s(0)\right|\left|U_3^s(x_3)\right|}} \quad [20]$$

where the subscript α follows the repeated index summation convention; the superscripts r,s index the incident- and scattered-wave modes (i.e., P, SV, SH, or their analogs in anisotropic media); s_i^r and s_n^s are corresponding depth-dependent, unit polarization vectors; $A^r(x_3)$ is the source amplitude, $U_3^r(x_3), U_3^s(x_3)$ are the vertical components of group velocity; and $\tau^r(x_3)$ and $\tau^s(x_3)$ are delay times of the incident and scattered modes, respectively.

The modal expansion allows us to isolate and describe individual scattering interactions; for example, we set $A^r(x_3) = 1/\sqrt{\rho(x_3)\left|U_3^r(x_3)\right|}$ for direct P-to-S scattering (say, $r=1$ and $s=2$), and the corresponding delay time functions are written as

$$\tau^r(x_3) = -\int_0^{x_3} \mathrm{d}y_3 p_3^P(y_3), \quad \tau^s(x_3,0) = \int_0^{x_3} \mathrm{d}y_3 p_3^S(y_3) \quad [21]$$

where $p_3^P(x_3)$ and $p_3^S(x_3)$ are the vertical components of phase slowness for P- and S-waves, respectively. The choice of $\tau^r(x_3)$ in the preceding text implies a time normalization where the direct P-wave ($r=1$) arrives at the Earth's surface at $\tau^r = 0$ consistent with the output of most deconvolution schemes described in Sections 1.08.3.3–1.08.3.5. Back scattering that involves free-surface reflection of the upgoing incident wave can be described through an alternate set of amplitude and delay time functions. For example, pure P-mode reflection (say, $r=2$ and $s=1$) is characterized by $A^r(x_3) = \widetilde{R}^{PP}/\sqrt{\rho(x_3)\left|U_3^r(x_3)\right|}$ where $\widetilde{R}^{PP}$ is the free-surface P-to-P reflection coefficient and the delay time functions are

$$\tau^r(x_3) = \int_0^{x_3} \mathrm{d}y_3 p_3^P(y_3), \quad \tau^s(x_3,0) = \int_0^{x_3} \mathrm{d}y_3 p_3^P(y_3) \quad [22]$$

(note that for an anisotropic reference medium that does not exhibit mirror symmetry, we would have to employ different values for up- and downgoing phase slowness in eqns [22]).

Inserting expressions [19] and [20] into [18] and retaining only the leading-order terms in frequency, one obtains

$$\Delta u_n(\mathbf{x}',\omega) \approx \sum_r\sum_s s_n^s(0)\mathrm{e}^{\mathrm{i}\omega p_\alpha x'_\alpha}\int \mathrm{d}x_3 B^{rs}(x_3,\omega) \left[\frac{\Delta c_{ijkl}}{\rho^0}s_l^r p_k^r s_i^s p_j^s + \frac{\Delta\rho}{\rho^0}s_i^r s_i^s\right]\mathrm{e}^{\mathrm{i}\omega(\tau^r(x_3)+\tau^s(x_3,0))} \quad [23]$$

where, for brevity, we have suppressed the x_3 dependence in all quantities within the square brackets, p_i^r, p_i^s are the phase slowness vectors of the incident- and scattered-wave fields at depth x_3, and the factor $B^{rs}(x_3,\omega)$ is defined by

$$B^{rs}(x_3,\omega) = -\frac{\mathrm{i}\omega A^r(x_3)\sqrt{\rho^0(x_3)}}{2\sqrt{\rho^0(0)\left|U_3^s(0)\right|\left|U_3^r(x_3)\right|}} \quad [24]$$

Equation [23] represents an asymptotic, linearized relation between the scattered field $\Delta u_n(0)$ measured at the Earth's surface and the unknown material parameters $\Delta c_{ijkl}(x_3)$ and $\Delta\rho(x_3)$. To simplify the extraction of these parameters, we follow Burridge et al. (1998) and define a fourth rank tensor a_{ijkl} that possesses the same symmetry properties as Δc_{ijkl} and satisfies

$$\frac{\Delta c_{ijkl}}{V^r V^s}a_{ijkl} = \Delta c_{ijkl}s_l^r p_k^r s_i^s p_j^s \quad [25]$$

where V^r and V^s represent the phase velocities of incident and scattered modes, respectively, averaged over all angles, that is

$$a_{ijkl} = \frac{V^r V^s}{8}\left[\left(s_i^s p_j^s + s_j^s p_i^s\right)\left(s_k^r p_l^r + s_l^r p_k^r\right) + \left(s_k^s p_l^s + s_l^s p_k^s\right)\left(s_i^r p_j^r + s_j^r p_i^r\right)\right] \quad [26]$$

This construction allows us to adopt a more compact notation and rewrite eqn [23] as

$$\Delta u_n(0,\omega) \approx \sum_r\sum_s s_n^s(0)\mathrm{e}^{\mathrm{i}\omega p_\alpha x'_\alpha}\int \mathrm{d}x_3 B^{rs}(x_3,\omega)\mathrm{e}^{\mathrm{i}\omega(\tau^r(x_3)+\tau^s(x_3,0))}\mathsf{w}^{\mathrm{T}}\Delta\mathsf{c} \quad [27]$$

The radiation patterns and material property perturbations are now contained within 22-element vectors, w and Δc, whose entries correspond to the 21 independent elastic constants and density as

$$\mathsf{w} \leftrightarrow \left[a_{ijkl}, s_i^s s_i^r\right], \quad \Delta\mathsf{c} \leftrightarrow \left[\frac{\Delta c_{ijkl}}{\rho^0}, \frac{\Delta\rho}{\rho^0}\right] \quad [28]$$

Equation [27] takes a form that may be readily discretized and solved for Δc. It is common practice, however, to consider the contribution of each scattering mode $\Delta u_i^{rs}(0,\omega)$ (where $\Delta u_i(\mathbf{x},\omega) = \sum_r\sum_s \Delta u_i^{rs}(\mathbf{x},\omega)$), independently. Assuming that the individual $\Delta u_i^{rs}(\mathbf{x},\omega)$ can be approximately isolated (see Section 1.08.6 for further discussion on this assumption), we define the scalar, time-domain quantity

$$f^{rs}(t) = \mathcal{F}^{-1}\left\{\frac{\Delta u_i^{rs}(0,\omega)s_i^s(0)\mathrm{e}^{-\mathrm{i}\omega p_\alpha x'_\alpha}}{B^{rs}(x_3,\omega)}\right\}\left[p_3^s(x_3) + p_3^r(x_3)\right] \quad [29]$$

where $\mathcal{F}^{-1}$ denotes, as before, inverse Fourier transformation. Note that contraction with $s_i^s(0)$ rotates the data into the

anticipated polarization direction of the upgoing scattered mode s. In practice, we accomplish this operation using eqn [2] since the effect of the free surface on polarization of the recorded wave field is not explicitly accounted for in the treatment of this section. Multiplication by $e^{-i\omega p_\alpha x'_\alpha}$ in eqn [29] removes the time shift associated with horizontal coordinate such that the arrival of the direct wave (P for $r=1$ and S for $r=2, 3$) corresponds to time 0. By inserting the expression for $\Delta u_i^{rs}(0,\omega)$ in eqns [27] into [29] and evaluating both integrals in ω and x_3 (with the aid of Leibniz' rule), we arrive at

$$f^{rs}(t=\tau^r(x_3)+\tau^s(x_3,0))=\mathbf{w}^{\mathrm{T}}(x_3)\Delta\mathbf{c}(x_3) \qquad [30]$$

that is, a one-to-one relation between material property perturbations at depth x_3 and the value of $f^{rs}(t)$ evaluated at time $t=\tau^r(x_3)+\tau^s(x_3,0)$. If we now assemble a large number of data $u_i^{rs}(0,\omega)$ representing different scattering interactions r, s and geometries (as reflected in p_i^r and p_i^s), normalize as in eqn [29], and arrange these data in a column vector $\mathbf{f}$, a system of equations can be written as

$$\mathbf{f}(x_3)=\mathbf{W}(x_3)\Delta\mathbf{c}(x_3) \qquad [31]$$

where the transposed vectors $\mathbf{w}^{\mathrm{T}}$ form the rows of $\mathbf{W}$. The solution to this system of equations amounts to an amplitude versus slowness analysis of the scattering coefficient corresponding to depth x_3. Normalization of the upgoing wave field by $[p_3^s+p_3^r]/B^{rs}(x_3,\omega)$ in eqn [29] ensures that it is appropriately scaled and filtered such that the perturbation profile $\Delta\mathbf{c}(x_3)$ is, to within the single-scattering and high-frequency approximations, correctly recovered. If, instead, we wish to recover a profile of reflectivity (or, more precisely, the singular function of the discontinuity surface scaled to the amplitude of the perturbation; e.g., Bleistein, 1987), we must remove the factor $i\omega$ in eqn [24]. In so doing, the solution of eqn [31] is seen to be simply a weighted diffraction stack of the data along move-out curves corresponding to the various scattering interactions r,s within the 1-D reference medium.

In the case of isotropic stratification, the reflectivity inversion affords a formal justification for the delay-and-sum approach introduced by Vinnik in his analysis of P-to-S conversions from the mantle transition zone in 1977 and adopted subsequently by numerous workers (e.g., Bostock, 1996; Chevrot et al., 1999; Dueker and Sheehan, 1998; Kind and Vinnik, 1988; Stammler et al., 1992). In these studies, data are stacked along move-out curves computed for a 1-D Earth model and corresponding to a range of trial depths, to produce a map of stacked amplitude as a function of delay time and discontinuity depth. If amplitude extrema are observed at delay times consistent with a trial depth, a discontinuity is tentatively identified (see **Figure 6**). An approximate reflectivity (or 'convertibility') depth profile can be recovered by slicing through the amplitude map along the appropriate travel-time curve (see **Figure 7**). This empirical approach is equivalent to migrating (or 'squeezing and stretching') traces to depth prior to stacking (e.g., Fee and Dueker, 2004; Gilbert et al., 2003). It handles kinematics in precisely the same way as the solution of eqn [31]. The dynamics are of secondary importance, and their neglect in empirical migration approaches only means that the stacked waveforms are less directly interpretable in terms of perturbations in the Earth's material properties. The creation of an amplitude map has the advantage of permitting visual

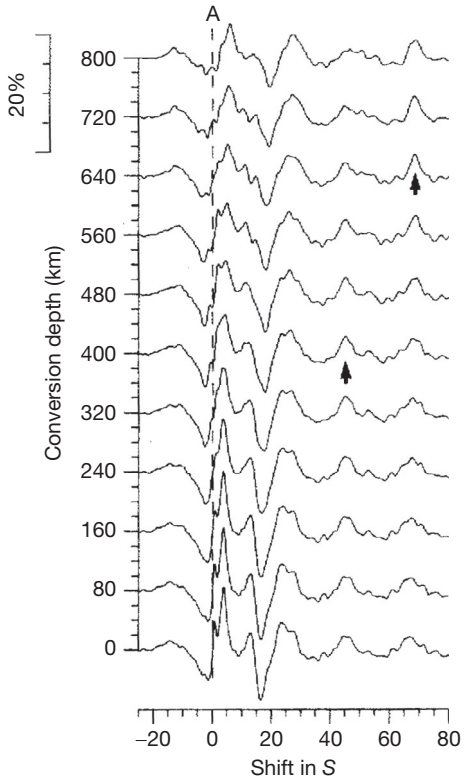

Figure 6 Delayed and summed *SV*-components of source-normalized teleseismic *P* recorded at the Gräfenberg array, Germany. Each trace represents a sum of seismograms, from events at different epicentral distances, delayed by a time interval corresponding to the expected arrival of a conversion from a given trial depth. Arrows point to amplitude maxima that occur for trial depths of 400 and 640 km and that are therefore consistent with the origin of *P*-to-*S* conversions from the two major transition zone discontinuities. Reproduced from Kind R and Vinnik LP (1988) The upper-mantle discontinuities underneath the GRF array from *P*-to-*SV* converted phases. *Journal of Geophysics* 62: 138–147.

assessment of the veracity of a potential structural signal on the basis of whether its amplitude maximum occurs at or near the expected travel time. In this sense, Vinnik's approach has much in common with the velocity spectrum stack developed for exploration applications and also applied to teleseismic wave fields by Gurrola et al. (1994). In this case, amplitude maxima of delayed and stacked waveforms are used to provide improved velocity (or in the case of teleseismic P-to-S conversions, Poisson's ratio) model information for structural imaging.

The method of Zhu and Kanamori (2000); following on Zandt and Ammon (1995) employs a similar approach to more tightly constrain crustal properties beneath a single three-component station, namely, depth of Moho and crustal Poisson's ratio, under the assumption that the latter is constant. This approach is commonly used for reconnaissance work (e.g., Darbyshire et al., 2007; Finotello et al., 2011; Phillips et al., 2012; Wei et al., 2011) and involves stacking of multiple-scattering modes r, s (consistent with the formulation in eqn [31]) along predicted travel-time trajectories for a grid of Moho depths and Poisson's ratios, to recover an

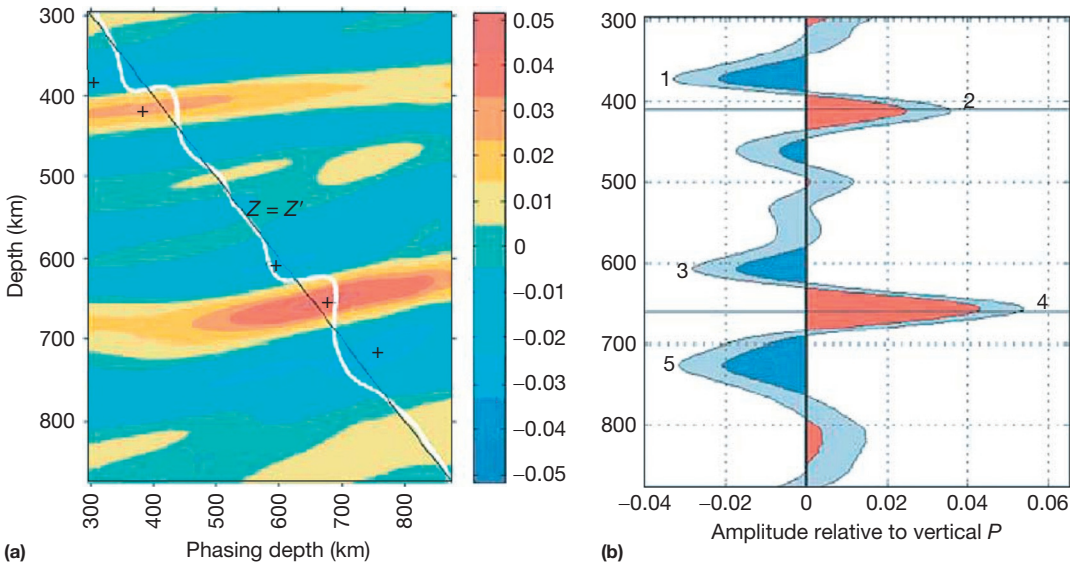

Figure 7 1-D migration (reproduced from Fee D and Dueker K (2004) Mantle transition zone topography and structure beneath the Yellowstone hotspot. *Geophysical Research Letters* 31: L18603. http://dx.doi.org/10.1029/2004GL020636). (a) Left panel shows amplitude map that results from stacking data along move-out curves corresponding to a range of conversion (phasing) depths. The vertical depth axis is proportional to time as mapped through a 1-D velocity model. (b) Right panel plots a slice through the 45° line shown in (a) and accomplishes a 1-D migrated depth profile of 'convertibility' below the Yellowstone hotspot.

optimal model under an assumed *P*-velocity. Extensions include applications to other layered regimes (e.g., subducting oceanic crust (Audet et al., 2009), lower crustal eclogites (Wittlinger et al., 2009), mantle transition zone (Schaeffer and Bostock, 2010), and the base of ice sheets (Wittlinger and Farra, 2012); the retrieval of absolute velocity information (e.g., Bostock and Kumar, 2010; Kumar and Bostock, 2008; Wittlinger et al., 2009); and the extraction of Poisson's ratio without prior knowledge of *P*-velocity (Helffrich and Thompson, 2010)).

Previous empirical studies of anisotropic stratification using scattered teleseismic wave fields can also be related to the linearized, 1-D inverse-scattering solution in eqn [31]. In this case, the Earth's response not only is simply a function of epicentral distance (or, more precisely, the magnitude of horizontal slowness, $\sqrt{p_\alpha p_\alpha}$) but also depends on back azimuth. Various authors (Bostock, 1997, 1998; Farra and Vinnik, 2000; Farra et al., 1991; Kosarev et al., 1984; Levin and Park, 1997, 1998; Vinnik and Montagner, 1996; Wilson et al., 2004) have noted that the back-azimuthal response of a stratified medium exhibiting different classes of anisotropic symmetry and orientation can be represented in simple trigonometric terms. Consequently, several schemes involving stacking with trigonometric weights have been proposed to investigate anisotropic stratigraphy. These schemes can be related to eqn [31] by noting that the linear system, for general Δc and typical teleseismic data sets, will be rank-deficient. It will thus be necessary to solve eqn [31] via a pseudoinverse (e.g., Bank and Bostock, 2003) with singular value decomposition being an obvious and tractable choice. These latter authors noted that only five- to seven-parameter combinations of Δc are likely to be resolvable using teleseismic *P* and that these parameter combinations can be identified with different harmonic orders of response in back azimuth θ, notably 1θ, 2θ, and 3θ. Recovery of Δc through eqn [31] thus amounts once more to a weighted diffraction stack and holds the advantage over more empirical schemes that the full data sensitivity to the elastic stiffness tensor is exploited without having to resort to simplified a priori model representations (e.g., hexagonal symmetry).

Finally, we remark that, in practice, it is difficult to isolate the individual scattering-mode contributions, $\Delta u^{rs}(\mathbf{x}, \omega)$, and in general, we will approximate these quantities by the observed wave field, $\Delta u(\mathbf{x}, \omega)$, for each scattering-mode interaction. The main drawback with this course of action is that we interpret a superposition of several different styles of scattering interaction *r*, *s* as that due to a single one with the result that artificial structures appear in the solution. The most commonplace example is the misinterpretation of the free-surface-reflected, back-scattered waves from shallow interfaces for direct, forward-scattered conversions from deeper interfaces. This shortcoming afflicts both 1-D and multidimensional analyses of teleseismic waves, and we shall comment on a potential remedy in **Section 1.08.6**.

1.08.5 Multidimensional Inversion

There are several approaches to consider in moving from 1-D to multiple dimensions. The first and simplest strategy is to assume that the Earth's structure varies slowly in the horizontal coordinates in which case a 2-D or 3-D profile can be assembled as a cascade of local 1-D models determined from individual, adjacent stations (e.g., Kumar et al., 2005). If stations are sufficiently closely spaced that the (1-D) ray paths of scattered phases intersect below the profile, it becomes advantageous to consider a 2-D model where scattered energy on seismogram is mapped to common conversion points (CCP) assuming a locally horizontal, plane-layer scattering geometry

(e.g., Dueker and Sheehan, 1998; Ferris et al., 2003; Knapmeyer and Harjes, 2000; Kosarev et al., 1999; Niu et al., 2005; Schulte-Pelkum et al., 2005; Simmons and Gurrola, 2000; Zandt et al., 2004). Travel-time and polarity corrections to account for layer dip where structures remain quasiplanar, for example, in subduction zones, provide further improvement in imaging (e.g., Kawakatsu and Watada, 2007; Kawakatsu and Yoshioka, 2011; **Figure 8**). Such CCP stacking techniques are commonly employed because they place less stringent requirements on spatial sampling than formal multidimensional inversion schemes, but of course, their accuracy deteriorates as departures from one-dimensionality or assumed planar structure become more pronounced.

Unlike the strictly 1-D case, the multidimensional inverse problem has not lent itself so readily to treatment using optimization via least squares because of the large increase in model parameters and concomitant rise in computations. It is likely, however, that in the near future, computational tractability will become less of a concern. Indeed, two recent studies (Frederiksen and Revenaugh, 2004; Wilson and Aster, 2005) have explored different least-squares formulations for solving multidimensional receiver function inversions, a trend that is likely to continue. Much of the essential machinery for this task has already been developed for exploration applications; we note, in particular, the work of Tarantola (1984, 1986).

The 1-D, high-frequency, Born-approximate inverse solution described in the previous section can, however, be efficiently extended to multiple dimensions so as to be computationally tractable on standard desktop computers. In this extension, there are no conceptual difficulties in dealing with 2-D versus 3-D problems, although there are practical limitations, in particular, for data from temporary, portable deployments. More specifically, it is difficult at the current time to assemble numbers of instruments sufficient to ensure that the teleseismic wave field is sampled with sufficient areal density (and aperture) to avoid aliasing most of its useful spectrum. Two approaches may be taken to remedy this difficulty. One may seek to interpolate data to a finer spacing over an areal grid followed by 3-D inversion (Neal and Pavlis, 1999, 2001; Poppeliers and Pavlis, 2003a,b) or follow the lead of early exploration practice and adopt a 2-D inverse strategy under the assumption that a dominant geologic strike direction can be identified (Bostock et al., 2001). In the following, we summarize the approach taken by the latter authors, which can be regarded as a 2-D, isotropic extension of the 1-D treatment outlined in **Section 1.08.4.3**.

We begin with the linearized integral equation [18]. In the 1-D case, the invariance of material properties in horizontal coordinates together with the far-field (quasiplanar) nature of the incident-wave field $u_i^0(\mathbf{x},\omega)$ allowed us to adopt plane-wave expansions for the incident and scattered modes as in

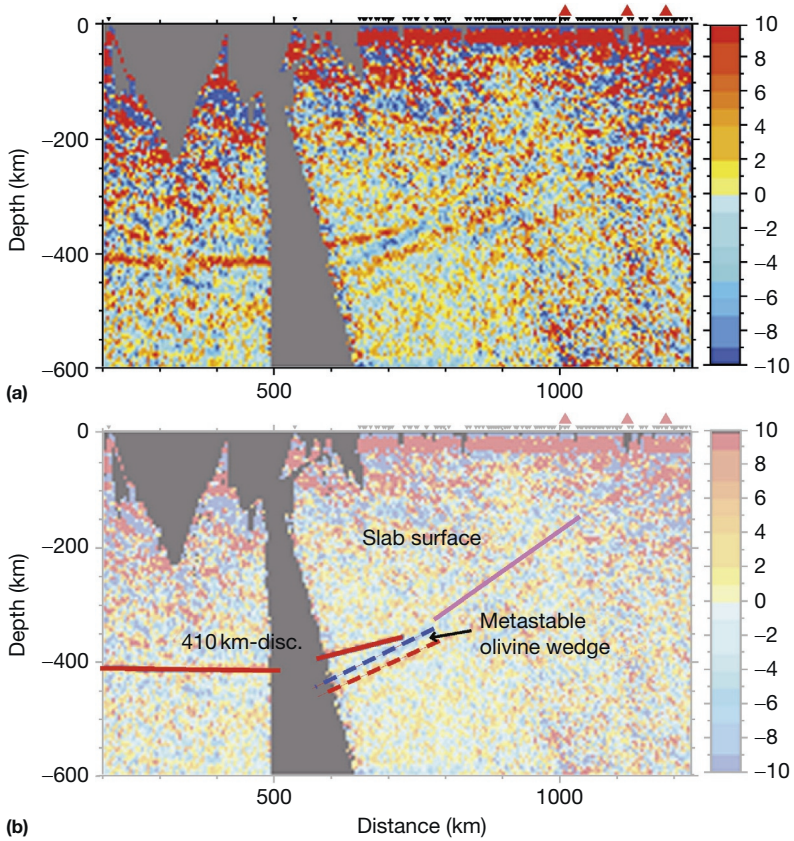

Figure 8 Common conversion point image (a) below southwest Japan with allowance made for assumed nonhorizontal geometry (reproduced from Kawakatsu H and Yoshioka S (2011) Metastable olivine wedge and deep dry cold slab beneath southwest Japan. *Earth and Planetary Science Letters* 303: 1–10). Image in (b) identifies structures associated with subducting Pacific Plate, metastable olivine wedge, and 400 km discontinuity.

eqns [19] and [20]. This choice is effectively equivalent to Fourier transforming over the horizontal plane. Accordingly, for a 2-D inversion where there is only one coordinate of spatial invariance, say, the strike coordinate x_2, we Fourier transform over this coordinate. We thereby assume that, for an incident (e.g., planar) wave field characterized by a single value of slowness p_2 in the strike direction, all resulting scattering interactions will be characterized by this same component of horizontal slowness, and so, we may parameterize the wave fields by this variable. Although not required, it will be computationally and practically expedient to assume that the reference medium is both 1-D and isotropic, so that the reference medium description is reduced from $c^0_{ijkl}(x_1, x_3), \rho^0(x_1, x_3)$ to, for example, $\alpha^0(x_3)$, $\beta^0(x_3)$, $\rho^0(x_3)$. Consequently, we may adopt the same 1-D form for the incident-wave field $u^0_i(\mathbf{x}, \omega)$, that is, eqn [19], whereas for the Green function, we adopt a form that allows for interaction with 2-D (i.e., line) scatterers:

$$G^0_{in}(\mathbf{x}, 0, \omega) = \sum_s \frac{1}{\sqrt{-\mathrm{i}\omega}} A^s\left(\mathbf{x}_\perp, \mathbf{x}'_\perp, p_2\right) \mathrm{e}^{\mathrm{i}\omega\left[p^s_1\left|x_1 - x'_1\right| - p_2 x_2 + \tau^s\left(\mathbf{x}_\perp, \mathbf{x}'_\perp\right)\right]} s^s_i(\mathbf{x}_\perp) s^s_n\left(\mathbf{x}'_\perp\right) \quad [32]$$

where, as before, $s = 1, 2, 3$ correspond to P, SV, and SH waves, respectively, and the 2-D amplitude functions A^s are defined, for example, for $s = 1$, as

$$A^s\left(\mathbf{x}_\perp, \mathbf{x}'_\perp, p_2\right) = \frac{1}{4\alpha^0(0)} \sqrt{\frac{2}{\pi\rho^0(x_3)\alpha^0(x_3)\rho^0(0)\left[J^P\left(\mathbf{x}_\perp, \mathbf{x}'_\perp, p_2\right)\right]^2 \sqrt{1 - p_2^2\left[\alpha^0(0)\right]^2}}} \quad [33]$$

with a comparable expression holding for the S-modes (i.e., $s = 2, 3$). We employ $\mathbf{x}_\perp = (x_1, x_3)$ to represent observation coordinates within the plane of 2-D spatial variations and evaluate source coordinates $\mathbf{x}_\perp{}'$ along the Earth's surface, that is, $\mathbf{x}_\perp{}' = (x_1{}', 0)$. The travel-time functions $\tau^s(\mathbf{x}_\perp, \mathbf{x}_\perp{}')$ are computed as in eqn [21], but now, we recognize that p^s_1 is no longer constant but depends on $x_1 - x_1{}'$. A similar consideration also applies in the definition of the unit polarization vectors $s^s_n(\mathbf{x}_\perp)$. The 2-D geometric spreading functions $J^s(\mathbf{x}_\perp, \mathbf{x}_\perp{}', p_2)$ $(= J^P(\mathbf{x}_\perp, \mathbf{x}_\perp{}', p_2)$, for $s = 1$, see, e.g., Hudson, 1980), depend on the divergence of the rays in the x_1, x_3 plane. Note that we have permitted an oblique component of incidence through dependence on x_2, p_2, which bears important practical implications as it will allow us to employ a full range of earthquake sources that need not align with the 2-D model geometry. If forms eqns [19] and [32] are inserted within the isotropic equivalent of eqn [18], we may construct 2-D, high-frequency, single-scattering, forward-modeling equations for various incident-/scattering-mode combinations r, s of the form

$$\Delta u_n\left(\mathbf{x}'_\perp, p_2, \omega\right) = \sum_r \sum_s s^s_n\left(\mathbf{x}'_\perp\right) \int \mathrm{d}\mathbf{x}_\perp F^{rs}(\mathbf{x}_\perp, \theta) A^r(x_3) A^s\left(\mathbf{x}_\perp, \mathbf{x}'_\perp, p_2\right) \mathrm{e}^{\mathrm{i}\omega\left(\tau^r(x_3) + \tau^s\left(\mathbf{x}_\perp, \mathbf{x}'_\perp\right)\right)} \quad [34]$$

The 2-D 'scattering potential,' $F^{rs}(\mathbf{x}_\perp, \theta)$, is derived from contractions of the stiffness tensor (expressed in terms of, e.g., velocities and density) and the local polarization and slowness vectors of the incident and scattered waves. It is expressed as a function of the scattering angle, $\theta = \theta^{rs}(\mathbf{x}_\perp, \mathbf{x}_\perp{}')$, between the slowness vectors of these two wave fields (see Figure 9), and the material property perturbations such that for, for example, forward P-to-S conversions ($r = 1$, $s = 2$)

$$F^{rs}(\mathbf{x}_\perp, \theta) = \rho^0\left[\frac{\Delta\beta}{\beta^0}\left(2\frac{\beta^0}{\alpha^0}\sin 2\theta\right) + \frac{\Delta\rho}{\rho^0}\left(\sin\theta + \frac{\beta^0}{\alpha^0}\sin 2\theta\right)\right] \quad [35]$$

where the dependence of the material property perturbations is, for example, $\Delta\beta = \Delta\beta(\mathbf{x}_\perp)$. Similar relations can be written for other combinations of scattering interaction r, s (see, e.g., Bostock et al., 2001).

The inverse problem can be tackled by applying an inverse Fourier transform to eqn [34], that is,

$$\Delta u_n\left(\mathbf{x}'_\perp, p_2, t\right) = \frac{1}{2\pi} \sum_r \sum_s s^s_n\left(\mathbf{x}'_\perp\right) \int \mathrm{d}\mathbf{x}_\perp F^{rs}(\mathbf{x}_\perp, \theta) A^r(x_3) A^s\left(\mathbf{x}_\perp, \mathbf{x}'_\perp, p_2\right) \delta\left(t - \tau^r(x_3) - \tau^s\left(\mathbf{x}_\perp, \mathbf{x}'_\perp\right)\right) \quad [36]$$

and noting that the result bears a close resemblance to the definition of the 2-D Radon transform $F(\mathbf{n}, t)$ of a function $f(\mathbf{x}_\perp)$ (Deans, 1983; Miller et al., 1987)

$$F(\mathbf{n}, t) = \int \mathrm{d}\mathbf{x}_\perp f(\mathbf{x}_\perp) \delta(t - \mathbf{n} \cdot \mathbf{x}_\perp) \quad [37]$$

where $\mathbf{n}$ is a unit vector in the 2-D plane defined by $\mathbf{x}_\perp$, especially if we restrict attention to a single-scattering mode $\Delta u^{rs}_n(\mathbf{x}_\perp{}', p_2, t)$. Here, we identify the scattered field $\Delta u_n(\mathbf{x}_\perp{}', p_2, t)$ with $F(\mathbf{n}, t)$ and the scattering potential $F^{rs}(\mathbf{x}_\perp, \theta)$ with $f(\mathbf{x}_\perp)$. The primary differences between the two equations are that the integrand in eqn [36] contains additional factors in the form $A^r(x_3)A^s(\mathbf{x}_\perp, \mathbf{x}_\perp{}', p_2)$ and that the arguments of the delta-function are not straight lines but, rather, isochronal curves along which the sum $\tau^r(x_3) + \tau^s(\mathbf{x}_\perp, \mathbf{x}_\perp{}')$ is constant. The correspondence can be made closer still by recognizing that the product of geometric amplitudes will, in general, be slowly varying and that, in keeping with the asymptotic forms adopted in eqns [19] and [32], the isochronal curves can be approximated

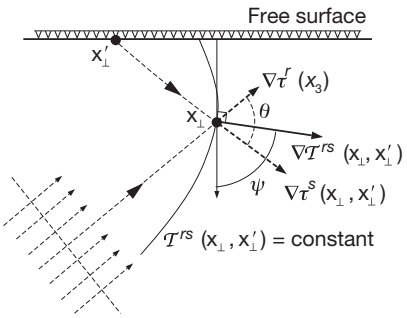

Figure 9 Geometric quantities relevant to high-frequency, inverse scattering of teleseismic wave fields for 2-D structure. The vectors $\nabla\tau_r$ and $\nabla\tau^s$ are the slowness vectors for the incident and scattered waves, respectively, whereas θ is the 'scattering' angle between them. The total slowness vector $\nabla\mathcal{T}^{rs} = \nabla\tau^r + \nabla\tau^s$, characterized by angle ψ, plays an important role in controlling spatial resolution within the generalized Radon transform.

locally as planar. We may then draw upon the formal inverse Radon transform (Beylkin, 1985; Beylkin and Burridge, 1990; Deans, 1983; Miller et al., 1987):

$$\begin{aligned} f(\mathbf{x}'_\perp) &= -\frac{1}{4\pi}\int \mathrm{d}\mathbf{n}\mathcal{H}\left\{\frac{\partial}{\partial t}F(\mathbf{n},t)\right\}\Big|_{t=\mathbf{n}\cdot\mathbf{x}'} \\ &= -\frac{1}{4\pi}\int \mathrm{d}\mathbf{n}\int \mathrm{d}\mathbf{x}_\perp f(\mathbf{x})\mathcal{H}\left\{\delta'\left(\mathbf{n}\cdot\left(\mathbf{x}'_\perp-\mathbf{x}_\perp\right)\right)\right\} \\ &= -\frac{1}{4\pi}\int \mathrm{d}\psi\int \mathrm{d}\mathbf{x}_\perp f(\mathbf{x})\mathcal{H}\left\{\delta'\left(\mathbf{n}\cdot\left(\mathbf{x}'_\perp-\mathbf{x}_\perp\right)\right)\right\} \end{aligned} \quad [38]$$

where ψ is the angle of $\mathbf{n}$, $\mathcal{H}\{\ \}$ denotes Hilbert transform, and $\delta'(x)$ is the derivative of $\delta(x)$, to devise a formal back-projection operator for the recovery of $F^{rs}(\mathbf{x}_\perp, \theta)$, namely,

$$F^{rs}(\mathbf{x}_\perp,\theta) \approx \frac{1}{4\pi}\int \mathrm{d}\psi \frac{|\nabla\mathcal{T}^{rs}|^2}{\sum_n \mathcal{A}_n^{rs}\mathcal{A}_n^{rs}}\sum_n \mathcal{A}_n^{rs} v_n^{rs}\left(\mathbf{x}'_\perp, p_2, t=\mathcal{T}^{rs}\left(\mathbf{x}_\perp,\mathbf{x}'_\perp\right)\right) \quad [39]$$

Here, we have, for brevity, defined the composite quantities

$$\begin{aligned} \mathcal{T}^{rs}\left(\mathbf{x}_\perp,\mathbf{x}'_\perp\right) &= \tau^r(x_3)+\tau^s\left(\mathbf{x}_\perp,\mathbf{x}'_\perp\right) \quad \mathcal{A}_n^{rs} \\ &= A^r(x_3)A^s\left(\mathbf{x}_\perp,\mathbf{x}'_\perp,p_2\right)s_n^s\left(\mathbf{x}'_\perp\right) \end{aligned} \quad [40]$$

and have identified $\nabla\mathcal{T}^{rs}\left(\mathbf{x}_\perp,\mathbf{x}'_\perp\right)/\left|\nabla\mathcal{T}^{rs}\left(\mathbf{x}_\perp,\mathbf{x}'_\perp\right)\right|$ with $\mathbf{n}$. Thus, the integration variable ψ is the angle of $\nabla\mathcal{T}^{rs}\left(\mathbf{x}_\perp,\mathbf{x}'_\perp\right)$, that is,

$$\psi = a\tan\frac{\partial_3\mathcal{T}^{rs}\left(\mathbf{x}_\perp,\mathbf{x}'_\perp\right)}{\partial_1\mathcal{T}^{rs}\left(\mathbf{x}_\perp,\mathbf{x}'_\perp\right)} \quad [41]$$

and the scattered-wave field is represented through the time series

$$v_n^{rs}\left(\mathbf{x}'_\perp,p_2,t\right) = \mathcal{F}^{-1}\left\{\Delta u_n^{rs}\left(\mathbf{x}'_\perp,p_2,\omega\right)\frac{-\mathrm{isgn}(\omega)}{\sqrt{-\mathrm{i}\omega}}\right\} \quad [42]$$

The geometric relationships among the various quantities defined in the preceding text are illustrated in **Figure 9**. As for the 1-D case, we have assumed that we are able to separate the recorded wave field into its individual scattering mode (r, s) contributions $\Delta u_n^{rs}(\mathbf{x}'_\perp, p_2, \omega)$. From eqn [39], we note that the scattering potential can be approximately recovered as a weighted diffraction stack of filtered data $v_n^{rs}(\mathbf{x}'_\perp, p_2, t)$ over the isochronal travel-time curves. The form of filter $-\mathrm{isgn}(\omega)/\sqrt{-\mathrm{i}\omega}$ applied to the scattered-wave field data in eqn [42] stems from the plane-wave/2-D geometry and ensures that, for example, a step function perturbation is recovered in the case of a discontinuity in material properties. Recovery of $F^{rs}(\mathbf{x}_\perp, \theta)$ is, of course, an intermediate result from which we wish to resolve the individual material property perturbations $\Delta\mathsf{c}(\mathbf{x}_\perp) = \left[\Delta\alpha/\alpha, \Delta\beta/\beta^0, \Delta\rho/\rho^0\right]^{\mathrm{T}}$. Exploiting the linear relation in eqn [35], this task is readily accomplished by assembling measurements of $F^{rs}(\mathbf{x}_\perp, \theta)$ for all available scattering interactions at a given model point within a column vector $\mathsf{f}(\mathbf{x}_\perp, \theta)$ and solving the trivial 3×3 system

$$\mathsf{f}(\mathbf{x}_\perp,\theta) = \mathsf{W}(\theta)\Delta\mathsf{c}(\mathbf{x}_\perp) \quad [43]$$

where, as in eqn [31], the row vectors constituting the matrix W represent radiation patterns for the various scattering-mode combinations r, s.

The main computational effort in this approach is expended in computing the weighted diffraction stack in eqn [39]. The appearance of $|\nabla\mathcal{T}^{rs}|^2$ as a weight in that equation corresponds to the factor $[p_3^s(x_3)+p_3^r(x_3)]$ in eqn [29] for the 1-D case. It represents the sensitivity of travel time to scatterer position and, as a product with frequency ω, governs the scale of resolution. For example, back-scattered modes, for which $|\nabla\mathcal{T}^{rs}|^2$ is in general large, possess better resolving capability than forward-scattered waves since a given change in scatterer position has a larger effect on timing of the scattered arrival (see, e.g., Rondenay et al., 2005). The direction of $\nabla\mathcal{T}^{rs}$, as quantified by dip angle ψ, controls the degree to which different structural dips can be resolved at a given model point. In contrast, material property resolution depends on the range of scattering angle θ afforded by the data and the different modal scattering sensitivities as represented through the radiation patterns (e.g., eqn [35]). Material property resolution may be analyzed through eigenvector decomposition of the matrix $\mathrm{W}^{\mathrm{T}}\mathrm{W}$ (e.g., Bostock and Rondenay, 1999; Forgues and Lambaré, 1992). Since teleseismic data are characterized by a limited range of θ, the simultaneous inversion of different scattering modes r, s affords the best prospects for discrimination of material properties.

In addition to the plane-wave, isotropic, 2-D oblique incidence geometry described in the preceding text, the generalized Radon transform treatment of the inverse-scattering problem has also been developed with point sources for acoustic waves (Miller et al., 1987), elastic waves in 3-D isotropic (Beylkin and Burridge, 1990), and anisotropic (Burridge et al., 1998) media. Like the 1-D case, these algorithms can be recast to recover singular functions of discontinuity surfaces (vs. Born-approximate perturbations), thereby accomplishing Kirchhoff-approximate inversion (Beylkin and Burridge, 1990; Bleistein, 1987; Bostock, 2002; de Hoop and Bleistein, 1997). In the teleseismic context, generalized Radon transform inversions have been strictly applied in a limited number of studies on subduction zones (Nicholson et al., 2005; Rondenay et al., 2001), Precambrian mobile belts (Poppeliers and Pavlis, 2003b; Rondenay et al., 2005), and the mantle transition zone (Liu and Pavlis, 2013).

If the weights in eqn [39] are ignored and otherwise normalized seismograms are simply stacked along move-out curves $t=\mathcal{T}^{rs}\left(\mathbf{x}_\perp,\mathbf{x}'_\perp\right)$, the formal parameter inversion is reduced to migration. Variants include migration via the Kirchhoff scattering integral (French, 1974; Schneider, 1978), which has been applied to the receiver (versus Green) functions with the aim of imaging (rather than inverting for) structure (e.g., Kind et al., 2002; Levander et al., 2005; Niu et al., 2005; Revenaugh, 1995; Sheehan et al., 2000; Wilson et al., 2005). All of the approaches mentioned in the preceding text can be classified as 'prestack' in that they deal directly with the individual Green function or receiver function data. Ryberg and Weber (2000) had described a teleseismic analogy to active source 'poststack' migration. This procedure involves normalizing teleseismic data to vertical incidence and stacking to produce a reduced data set, which can be readily processed using seismic reflection algorithms. Chen et al. (2005a) had built upon this poststack framework to develop a wave equation migration method that back propagates CCP stacked receiver functions into structural models and that has been applied to image the Japanese subduction zones (Chen et al., 2005b).

1.08.6 Beyond the Born Approximation

As argued in Sections 1.08.4 and 1.08.5, the tools of inverse scattering provide a framework for understanding many of the empirical approaches developed and employed over the past four decades to analyze scattered teleseismic wave fields in terms of lithospheric and upper mantle structure. In addition, the application of these techniques in recent years to multichannel data sets collected over, for example, plate boundaries, has led to new insights into the structures and dynamics of these complex regions that would have been difficult to achieve through a less complete analysis. As access to large numbers of instruments improves, it is possible that sampling of teleseismic wave fields may begin to approach that in exploration practice, allowing and prompting still more ambitious and complete treatments. Clearly, one approach is to employ fully numerical solutions (see Chapter 1.07) to model receiver-side scattering of teleseismic waves, and a number of authors have begun to investigate this route. Roecker et al. (2010) presented a spectral, finite-difference scheme to model plane-wave scattering in 2-D and demonstrated its incorporation within a waveform inversion using synthetic data. Monteiller et al. (2013) coupled 1-D global simulations with the spectral element method on a 3-D regional domain to compare numerical simulations with receiver function observations from the Pyrenees. As computational resources improve, regional waveform tomography employing, for example, adjoint methods (Tromp et al., 2005) will eventually become practical on a routine basis. An alternative approach to fully numerical treatments of the forward problem involves higher-order, nonlinear inverse scattering. We shall conclude this chapter by sketching out such a formulation, based on recent theoretical developments in reflection seismology, that would permit a nonlinear treatment of inverse scattering for teleseismic wave fields.

1.08.6.1 Shortcomings of the Born Approximation

Perhaps the most serious shortcomings of the methodologies heretofore described in Sections 1.08.4 and 1.08.5 lie in the linearization or 'Born approximation' made in eqn [18]. There are several negative consequences that follow from the Born approximation. First, as is widely appreciated, the reference medium must be sufficiently close to the real Earth to ensure that the phase of the wave fields is accurately represented. If not, images may become seriously distorted, usually through blurring, leading to reduced resolution and, worse, misinterpretation (see, e.g., Yilmaz, 2001). As researchers attempt to exploit higher frequencies in the teleseismic wave field (up to 10 Hz for teleseismic P generated by deep earthquakes), there will be increased need to improve reference velocity estimates.

A second drawback of the Born approximation is its failure to account for higher-order scattering in the form of multiple reflection/conversion. In reflection seismology, the most serious manifestation of multiple scattering is present in the form of free-surface multiples, which are order $O(\varepsilon^2)$ in amplitude. In the teleseismic context, the free-surface multiples are still larger ($O(\varepsilon)$) due to the transmission geometry as explained in Section 1.08.3.2 and have presented that a major impediment to lithospheric imaging due to the arrival of multiple signals from the Moho during the same time interval that directs conversions from the shallow mantle (say, 100–250 km depth) would be expected. Using formal inversion approaches, the multiples can be accommodated to varying degrees through the simultaneous inclusion of both direct and free-surface-reflected waves within the incident-wave field $u_i^0(\mathbf{x},\omega)$ as in eqn [19]. If, however, as we have advocated in coming to solutions for eqns [31] and [43], the approximation $\Delta u^{rs}(\mathbf{x},\ \omega)\approx\Delta u(\mathbf{x},\ \omega)$ is made for each mode combination r,s, this accommodation is incomplete and artificial structures resulting from misidentification of one scattering mode for another will occur (e.g., Shragge et al., 2001). Most studies based on diffraction stacking have implicitly adopted the $\Delta u^{rs}(\mathbf{x},\ \omega)\approx\Delta u(\mathbf{x},\ \omega)$ assumption for computational expedience. The advantage, as exemplified in the generalized Radon transform approach of the previous section (cf. eqn [43]), is that the matrix $\mathbf{W}^T\mathbf{W}$ is block-diagonal in structure leading to solution of a small (rank equivalent to number of material parameters considered) linear system for each spatial location within the model. If we choose, instead, to include both forward- and back-scattered (multiples) waves simultaneously and avoid the latter approximation, the Hessian becomes block-band-diagonal and computational expense increases dramatically. This latter approach is feasible using sparse matrix techniques, especially in 2-D, but to our knowledge has yet to be applied.

Notwithstanding the viability of simultaneously including the direct-wave and free-surface reflections within the definition of $u_i^0(\mathbf{x},\omega)$, there is reason to consider a formal decomposition of the observed field, $\Delta u_i(\mathbf{x},\ \omega)$, into individual scattering modes, $\Delta u_i^{rs}(\mathbf{x},\omega)$. Motivation for this line of thought stems from recent progress in reflection seismology by Weglein and coworkers (Matson, 1997; Weglein et al., 1997, 2003) and Wapenaar et al. (2004). Weglein's group has demonstrated that a sequential, task-driven approach, which includes isolation and removal of free-surface reflections, results in a better-posed, nonlinear treatment of the inverse-scattering problem within the seismic reflection context. Moreover, Wapenaar et al. had developed a theoretical framework based on correlational reciprocity (Bojarski, 1983) that allows the transformation of transmission (earthquake) data into reflection data, thereby effectively accomplishing the scattering-mode decomposition and allowing, in principle, the inversion of transmission data with reflection algorithms. In the following two subsections, we shall outline these procedures in more detail.

1.08.6.2 The Inverse-Scattering Series

Weglein and coworkers adopt operator-series representations to address both the forward- and inverse-scattering problems. The operator notation is convenient because it is largely independent of geometry and model type and affords a succinct summary of the main arguments. For further detail and background, the reader is referred to Weglein et al. (2003).

We begin with the operator form of the Lippman–Schwinger equation [15]:

$$\mathcal{U}=\mathcal{G}-\mathcal{G}^0=\mathcal{G}^0\mathcal{V}\mathcal{G} \qquad [44]$$

where we define $\mathcal{U}$ to be the data generation operator and $\mathcal{G}$ and $\mathcal{G}^0$ are the Green operators for the true Earth and reference

medium, respectively, that act on a given force distribution $f_i(\mathbf{x}, \omega)$ to produce a vector wave field. For example, in the teleseismic context, the scattered-wave field (cf. eqn [15]) can be written

$$\begin{aligned}\Delta u_i(\mathbf{x}, \omega) &= \mathcal{U}\{f_i\} = \mathcal{G}\{f_i\} - \mathcal{G}^0\{f_i\} \\ &= \int \mathrm{d}\mathbf{y}\left[G_{ij}(\mathbf{x}, \mathbf{y}, \omega) - G^0_{ij}(\mathbf{x}, \mathbf{y}, \omega)\right] f_j(\mathbf{y}, \omega)\end{aligned} \qquad [45]$$

where, as before, $G^0_{ij}(\mathbf{x}, \mathbf{y}, \omega)$ is the Green function for the reference medium (e.g., eqns [20] and [32] for laterally homogeneous reference media with 1-D and 2-D source geometries, respectively, in the high-frequency approximation); $G_{ij}(\mathbf{x}, \mathbf{y}, \omega)$ is the unknown Green function of the true Earth; and f_i then represents the force distribution that gives rise to upgoing, planar *P*- or *S*-wave fields in the absence of heterogeneity. The differential operator $\mathcal{V}$ includes the action of the material property perturbations and can be written as

$$\mathcal{V} = \partial_j \Delta c_{ijkl} \partial_k + \Delta\rho\omega^2 \delta_{il} \qquad [46]$$

Note that eqn [44] implies $\mathcal{G} = \mathcal{G}^0 + \mathcal{G}^0\mathcal{V}\mathcal{G}$ and so by successive insertion, we recover the forward-scattering series:

$$\mathcal{U} = \mathcal{G}^0\mathcal{V}\mathcal{G}^0 + \mathcal{G}^0\mathcal{V}\mathcal{G}^0\mathcal{V}\mathcal{G}^0 + \mathcal{G}^0\mathcal{V}\mathcal{G}^0\mathcal{V}\mathcal{G}^0\mathcal{V}\mathcal{G}^0 + \cdots \qquad [47]$$

From the RHS of eqn [47], we note that $\mathcal{G}$ is not required to solve the forward problem; that is, knowledge of $\mathcal{G}^0\{f_i\}$ is sufficient to recover $\mathcal{U}\{f_i\}$, if $\mathcal{V}$ is given.

The goal of the inverse problem is to isolate the scattering operator $\mathcal{V}$ (and from it Δc_{ijkl}, $\Delta\rho$) from the data generation operator $\mathcal{U}$ as represented by the data $\Delta u_i(\mathbf{x}, \omega)$ in eqn [45] using, again, knowledge of $\mathcal{G}^0$ alone. The inverse-scattering series solution represents $\mathcal{V}$ in series form as

$$\mathcal{V} = \mathcal{V}_1 + \mathcal{V}_2 + \mathcal{V}_3 + \mathcal{V}_4 + \cdots \qquad [48]$$

where the individual terms are organized in orders of the data $\mathcal{U}$. Inserting eqn [48] within [47] allows one to solve for these terms explicitly. For example, the first three equations are

$$\begin{aligned}\mathcal{U} &= \mathcal{G}^0\mathcal{V}_1\mathcal{G}^0 \\ 0 &= \mathcal{G}^0\mathcal{V}_2\mathcal{G}^0 + \mathcal{G}^0\mathcal{V}_1\mathcal{G}^0\mathcal{V}_1\mathcal{G}^0 \\ 0 &= \mathcal{G}^0\mathcal{V}_3\mathcal{G}^0 + \mathcal{G}^0\mathcal{V}_2\mathcal{G}^0\mathcal{V}_1\mathcal{G}^0 + \mathcal{G}^0\mathcal{V}_1\mathcal{G}^0\mathcal{V}_2\mathcal{G}^0 + \mathcal{G}^0\mathcal{V}_1\mathcal{G}^0\mathcal{V}_1\mathcal{G}^0\mathcal{V}_1\mathcal{G}^0\end{aligned} \qquad [49]$$

where we have used the fact that $\mathcal{U}$ is, by definition, first order in itself. In principle, these equations can be solved sequentially, first for $\mathcal{V}_1$, then for $\mathcal{V}_2$, and so on. Note that $\mathcal{V}_1$ is just the Born-approximate solution to the inverse problem, which may or may not accurately represent the true Earth (i.e., $\mathcal{V}$) depending on the proximity of $\mathcal{G}^0$ to $\mathcal{G}$.

Blind application of the series solution to raw data is marred by poor convergence properties and thus does not afford a practical solution to the inverse-scattering problem. Rather, Weglein et al. advocated that a 'subseries' approach be taken whereby sets of terms in the inverse series are identified with specific tasks and a sequential application is performed. This sequence of tasks is, namely, (i) removal of free-surface multiples, (ii) removal of internal multiples, (iii) imaging of scatterer location, and (iv) material property recovery. It has been noted that tasks (i) and (ii) can be effectively performed with absolutely no knowledge of the underlying velocity structure and with excellent convergence properties. Tasks (iii) and (iv) are the topic of current research and early results show promise (Weglein et al., 2002).

The relevance of the latter work to the teleseismic problem is twofold. First, it indicates that a sequential treatment that proceeds from multiple removal through material property inversion is likely to be better-posed than simultaneous solution. Second, as we sketch out in the succeeding text, it is possible, at least in principle, to transform the teleseismic transmission problem directly into a reflection problem such that the inverse-scattering series, as developed for exploration purposes, is then directly applicable.

1.08.6.3 Transmission to Reflection

Perhaps the most direct way of isolating individual scattering modes $\Delta u_i^{rs}(\mathbf{x}, \omega)$ is to consider reformulating the transmission problem as a reflection problem. Motivation for this concept stems from early work of Claerbout (1968) who demonstrated a relationship between the transmission response of a layered acoustic half-space and its reflection response. For precritical, energy flux-normalized elastic waves in 1-D media, this relation can be written

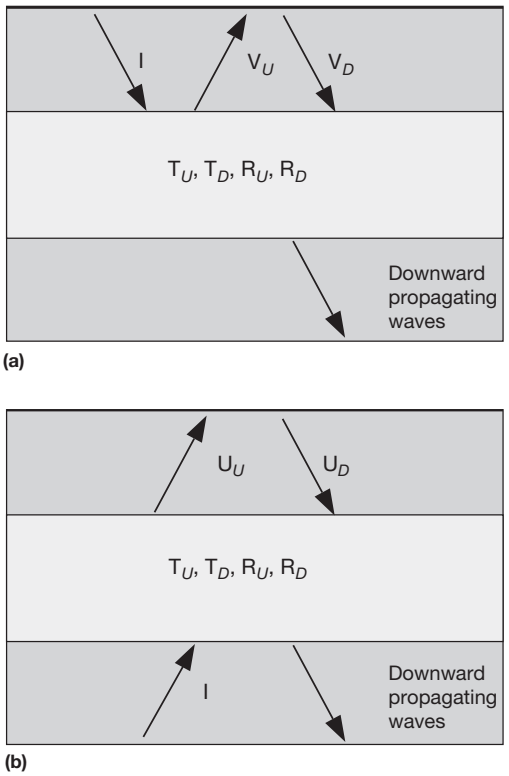

Figure 10 Geometric definition of quantities relevant to the transformation of transmission wave fields to reflection wave fields. (a) Reflection experiment: An incident-wave field (I) interacts with stratification from the preceding text to produce an upgoing wave field V_U and a downgoing wave field V_D at the Earth's free surface. (b) Transmission experiment: In this case, direct wave (I) is incident on stratification from below and produces upgoing (U_U) and downgoing (U_D) wave fields at the free surface.

$$\mathsf{U}^*\mathsf{U}^{\mathrm{T}} = \mathsf{I} + \mathsf{R}\mathsf{V} + \mathsf{V}^{\mathrm{H}}\mathsf{R}^{\mathrm{H}} \qquad [50]$$

where $\mathrm{U} = \mathrm{U}(\omega, \mathbf{p}_\perp)$ is the 3×3 matrix of eqn [8] containing the transmission response for different modes incident upon the base of a stratified half-space bounded in the preceding text by free surface, $\mathrm{V} = \mathrm{V}(\omega, \mathbf{p}_\perp)$ represents the corresponding reflection response for the same medium to different modes incident from earlier, $\tilde{\mathsf{R}} = \tilde{\mathsf{R}}(\mathbf{p}_\perp)$ is the free-surface reflection matrix, I is the identity matrix, and ^{H} denotes conjugate transpose. The two geometric configurations are illustrated in **Figure 10**.

Recall that complex conjugation in the frequency domain is equivalent to time reversal and that the inverse Fourier transforms of the elements of U and V are causal functions. Accordingly, each element on the left-hand side of eqn [50] represents, in the time domain, a sum of cross correlations and equates to the sum of a causal function $\left(\mathcal{F}^{-1}\left\{\tilde{\mathsf{R}}\mathsf{V}\right\}\right)$, an acausal function $\left(\mathcal{F}^{-1}\left\{\mathsf{V}^{\mathrm{H}}\tilde{\mathsf{R}}^{\mathrm{H}}\right\}\right)$ and, for diagonal elements, an impulse $\left(\mathcal{F}^{-1}\{\mathsf{I}\}\right)$ at zero lag. The time-domain reflection response $\mathcal{F}^{-1}\{\mathsf{V}\}$ can therefore be recovered by applying $\tilde{\mathsf{R}}^{-1}$ to $\mathcal{F}^{-1}\left\{\mathsf{U}^*\mathsf{U}^{\mathrm{T}}\right\}$ upon zeroing negative lags where, as in eqn [2], we have assumed that the near-surface material properties (and hence $\tilde{\mathsf{R}}$) are known. Since the individual elements of $\mathcal{F}^{-1}\{\mathsf{V}\}$ represent the reflection response of the stratified half-space to a separate incident mode, an isolation of different, first-order ($O(\varepsilon)$) modal interactions to individual components has therefore been achieved. **Figure 11** shows the result of this procedure applied to data from station HYB by Kumar and Bostock (2006) who outline a practical recipe for its implementation.

Note that the effect of the free surface is still included within V in as far as $O(\varepsilon^2)$ and higher-order, free-surface-related multiples are contained therein. The first step of the inverse-scattering series scheme involves removing these multiples. For 1-D, we accomplish this task by writing

$$\mathsf{V} = \mathsf{R}_D\left(\mathsf{I} - \tilde{\mathsf{R}}\mathsf{R}_D\right)^{-1} \qquad [51]$$

where we have, once more, employed the notation of Kennett (1983) and used R_D to denote the reflection matrix for the stratification alone (no free surface included). Reorganizing and solving for R_D using successive insertion leads to the series solution:

$$\mathsf{R}_D = \mathsf{V} - \mathsf{V}\tilde{\mathsf{R}}\mathsf{V} + \mathsf{V}\tilde{\mathsf{R}}\mathsf{V}\tilde{\mathsf{R}}\mathsf{V} - \mathsf{V}\tilde{\mathsf{R}}\mathsf{V}\tilde{\mathsf{R}}\mathsf{V}\tilde{\mathsf{R}}\mathsf{V} + \cdots \qquad [52]$$

Subsequent steps, including multiple elimination, spatial imaging, and material property recovery, are more involved, and the reader is referred to Weglein et al. (2003) for details and discussion.

The theory describing extension of the transmission-to-reflection transformation to multiple dimensions has recently been developed by Wapenaar et al. (2004) by exploiting correlational and convolutional reciprocity. Accordingly, the 3-D extension to eqn [50] expressed in the spatial (vs. slowness) domain becomes

$$\int_Z \mathrm{d}\mathbf{x}\,\mathsf{U}^*\left(\mathbf{x}'_A, \mathbf{x}, \omega\right)\mathsf{U}^{\mathrm{T}}\left(\mathbf{x}'_B, \mathbf{x}, \omega\right) = \mathsf{I}\delta\left(\mathbf{x}'_A - \mathbf{x}'_B\right) + \tilde{\mathsf{R}}\mathsf{V}\left(\mathbf{x}'_A, \mathbf{x}'_B, \omega\right) + \mathsf{V}^{\mathrm{H}}\left(\mathbf{x}'_A, \mathbf{x}'_B, \omega\right)\tilde{\mathsf{R}}^{\mathrm{H}} \qquad [53]$$

where, as before, the primed coordinates are located at the free surface, the surface integral over horizontal coordinate $\mathbf{x}$ is

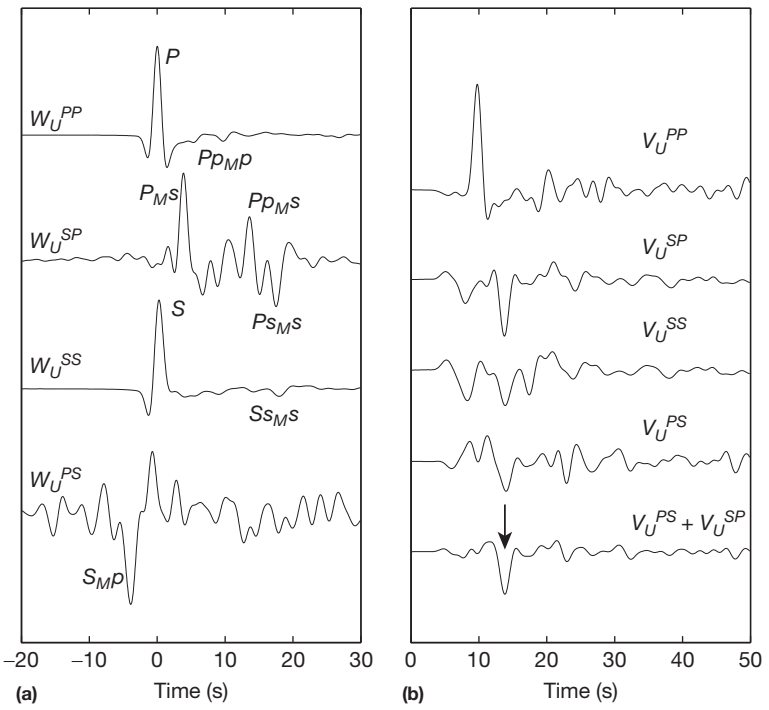

Figure 11 Transmission to reflection transformation of data from HYB (reproduced from Kumar MR and Bostock MG (2006) Transmission to reflection transformation of teleseismic wavefields. *Journal of Geophysical Research* 111: B08306). (a) Input transmission data. Components W_U^{PP} and W_U^{SP} were computed from teleseismic *P* data shown in **Figure 5** over the slowness range 0.04–0.0575 s km^{-1}, whereas components W_U^{PS} and W_U^{SS} were computed from *SKS* recordings over the same range. (b) Transformed reflection response. Note that bottom trace is computed as sum of $V_U^{PS} + V_U^{SP}$ since these two traces should, by reciprocity, be equivalent. Arrow indicates the reflection–conversion from the continental Moho.

evaluated at some depth Z below the heterogeneity, and the dependencies indicate that, for example, $\mathsf{V}(\mathbf{x}_A', \mathbf{x}_B', \omega)$ is the upgoing wave field recorded at surface location $\mathbf{x}_A'$ due to a source at surface location $\mathbf{x}_B'$, at frequency ω. Likewise, the multidimensional equivalent of eqn [51] can be written as

$$\mathsf{V}(\mathbf{x}_A', \mathbf{x}_B', \omega) = \mathsf{R}_D(\mathbf{x}_A', \mathbf{x}_B', \omega) + \int \mathrm{d}\mathbf{x}' \mathsf{R}_D(\mathbf{x}_A', \mathbf{x}', \omega) \widetilde{\mathsf{R}} \mathsf{V}(\mathbf{x}', \mathbf{x}_B', \omega) \quad [54]$$

The extension to multiple dimensions thus places greater demands on data by requiring the evaluation of surface integrals within certain depth ranges. It remains to be seen whether these demands can be accommodated through data interpolation/extrapolation in the teleseismic context where seismicity is sparse and irregularly distributed.

1.08.7 Conclusions

Over the past few decades, scattered teleseismic body waves have contributed greatly to our understanding of crust and mantle structure (see, e.g., **Chapters 1.16**, **1.21** and **1.24**). They possess higher resolving capability for small-scale structure than other elements of the global seismic wave train and do not suffer from the shallow depth sampling that limits active source seismic surveys. In this chapter, we have provided an overview of methodologies used to extract receiver-side structural information from the scattered teleseismic wave fields. These methodologies address two fundamental issues: (1) the isolation of structural signal from earthquake source signature and (2) the translation of structural signals into Earth models. The identification, in early practice, of source-free transfer functions formed by simple ratios of vector component waveforms has gradually given way in more recent work to better approximations to the true Earth 'Green function,' thereby extending sensitivity to the Earth's material parameters. In a like manner, the processing of these structural signals using empirical delay-and-sum approaches has progressed in the last few years to formal inversion where quantitative material property separation is, at least in principle, possible. These technological advances have brought analysis of scattered teleseismic waveforms in line with modern reflection seismic signal processing. In fact, as we have attempted to illustrate in the previous section, it is now possible to contemplate unified reflection/transmission approaches to the inverse-scattering problem. An important future challenge in application to global seismology will be to overcome the sparse sampling imposed by earthquake source distributions and current inventories of instrumentation.

References

Aki K and Richards PG (2002) *Quantitative Seismology*. Sausalito, CA: University Science Books.

Ammon CJ (1991) The isolation of receiver effects from teleseismic *P* waveforms. *Bulletin of the Seismological Society of America* 81: 2504–2510.

Ammon CJ, Randall GE, and Zandt G (1990) On the nonuniqueness of receiver function inversions. *Journal of Geophysical Research* 95: 15303–15318.

Amundsen L and Reitan A (1995) Decomposition of multicomponent sea-floor data into upgoing and downgoing *P*- and *S*-waves. *Geophysics* 60: 563–572.

Andrews DJ (1986) Objective determination of source parameters and similarity of earthquakes of different size. In: Das S, Boatwright J, and Scholz CH (eds.). *Earthquake Source Mechanics*, vol. 37, pp. 259–267. Washington, DC: American Geophysical Union.

Asencio E, Knapp JH, Owens TJ, and Helffrich G (2003) Mapping fine-scale heterogeneities within the continental mantle lithosphere beneath Scotland: Combining active- and passive-source seismology. *Geology* 31: 477–480.

Audet P, Bostock MG, Christensen NI, and Peacock SM (2009) Seismic evidence for overpressured subducted oceanic crust and megathrust fault sealing. *Nature* 457: 76–78.

Baag CE and Langston CA (1985) Shear-coupled PL. *Geophysical Journal of the Royal Astronomical Society* 80: 363–385.

Baig AM, Bostock MG, and Mercier J-P (2005) Spectral reconstruction of teleseismic *P* Green's Functions. *Journal of Geophysical Research* 110: B08306. http://dx.doi.org/10.1029/2003JB003625.

Bank C-G and Bostock M (2003) Linearized inverse scattering of teleseismic waves for anisotropic crust and mantle structure: 2. Numerical examples and application to data from Canadian stations. *Journal of Geophysical Research* 108. http://dx.doi.org/10.1029/2002JB001951.

Båth M and Stefánson R (1966) *S-P* conversion at the base of the crust. *Annals of Geophysics* 19: 119–130.

Baumgardt DR and Alexander SS (1984) Structure of the mantle beneath Montana Lasa from analysis of long-period, mode-converted phases. *Bulletin of the Seismological Society of America* 74: 1683–1703.

Beylkin G (1985) Imaging of discontinuities in the inverse scattering problems by inversion of causal generalized Radon transform. *Journal of Mathematical Physics* 26: 99–108.

Beylkin G and Burridge R (1990) Linearized inverse scattering problems in acoustics and elasticity. *Wave Motion* 11: 15–52.

Bleistein N (1987) On the imaging of reflectors in the earth. *Geophysics* 52: 931–942.

Bock G (1991) Long-period *S* to *P* converted waves and the onset of partial melting beneath Oahu, Hawaii. *Geophysical Research Letters* 18: 869–872.

Bock G (1994) Multiples as precursors to *S*, *SKS* and *ScS*. *Geophysical Journal International* 119: 421–427.

Bojarski NN (1983) Generalized reaction principles and reciprocity theorems for the wave equations, and the relationship between the time-advanced and time-retarded fields. *Journal of the Acoustical Society of America* 74: 281–285.

Bostock MG (1996) *Ps* conversions from the upper mantle transition zone beneath the Canadian landmass. *Journal of Geophysical Research* 101: 8393–8402.

Bostock MG (1997) Anisotropic upper mantle stratigraphy and architecture of the Slave craton. *Nature* 390: 392–395.

Bostock MG (1998) Mantle stratigraphy and evolution of the Slave province. *Journal of Geophysical Research* 103: 21183–21200.

Bostock MG (2002) Kirchhoff-approximate inversion of teleseismic wavefields. *Geophysical Journal International* 149: 787–795.

Bostock MG (2003) Linearized inverse scattering of teleseismic waves for anisotropic crust and mantle structure: 1. Theory. *Journal of Geophysical Research* 108: 2258. http://dx.doi.org/10.1029/2002JB001950.

Bostock MG (2004) Green's functions, source signatures, and the normalization of teleseismic wave fields. *Journal of Geophysical Research* 109: B03303. http://dx.doi.org/10.1029/2003B002783.

Bostock MG and Kumar MR (2010) Bias in seismic estimates of crustal properties. *Geophysical Journal International* 182: 403–407.

Bostock MG and Rondenay S (1999) Migration of scattered teleseismic body waves. *Geophysical Journal International* 137: 732–746.

Bostock MG, Rondenay S, and Shragge J (2001) Multiparameter two-dimensional inversion of scattered teleseismic body waves. 1. Theory for oblique incidence. *Journal of Geophysical Research* 106: 30771–30782.

Bostock M and Sacchi MD (1997) Deconvolution of teleseismic recordings for mantle structure. *Geophysical Journal International* 129: 143–152.

Bostock M and Tréhu AM (2012) Wave-field decomposition of ocean bottom seismograms. *Bulletin of Seismological Society of America* 102: 1681–1692.

Burdick LJ and Langston CA (1977) Modeling crustal structure through the use of converted phases in teleseismic body waveforms. *Bulletin of the Seismological Society of America* 67: 677–692.

Burridge R, de Hoop MV, Miller D, and Spencer C (1998) Multiparameter inversion in anisotropic elastic media. *Geophysical Journal International* 134: 757–777.

Chen L, Wen L, and Zheng T (2005a) A wave equation migration method for receiver function imaging. 1. Theory. *Journal of Geophysical Research* 110: B11309. http://dx.doi.org/10.1029/2005JB003665.

Chen L, Wen L, and Zheng T (2005b) A wave equation migration method for receiver function imaging. 2. Application to the Japan subduction zone. *Journal of Geophysical Research* 110: B11310. http://dx.doi.org/10.1029/2005JB003666.

Chevrot S, Vinnik LP, and Montagner J-P (1999) Global-scale analysis of mantle *Ps* phases. *Journal of Geophysical Research* 104: 20203–20219.

Claerbout JF (1968) Synthesis of a layered medium from its acoustic transmission response. *Geophysics* 33: 264–269.

Claerbout JF (1976) *Fundamentals of Geophysical Data Processing*. New York, NY: McGraw-Hill.

Clayton RW and Wiggins RA (1976) Source shape estimation and deconvolution of teleseismic body waves. *Geophysical Journal International* 103: 301–320.

Clitheroe G, Gudmundsson O, and Kennett BLN (2000) The crustal thickness of Australia. *Journal of Geophysical Research* 105: 13697–13713.

Darbyshire FA, Eaton DW, Frederiksen AW, and Ertolahti L (2007) New insights into the lithosphere beneath the Superior Province from Rayleigh wave dispersion and receiver function analysis. *Geophysical Journal International* 169: 1043–1068.

de Hoop MV and Bleistein N (1997) Generalized Radon transform inversions for reflectivity in anisotropic elastic media. *Inverse Problems* 13: 669–690.

Deans SR (1983) *The Radon Transform and some of its Applications*. New York, NY: Wiley.

Dueker KG and Sheehan AF (1998) Mantle discontinuity structure beneath the Colorado Rocky Mountains and High Plains. *Journal of Geophysical Research* 103: 7153–7169.

Eaton DW, Darbyshire F, Evans RL, Grütter H, Jones AG, and Yuan X (2009) The elusive lithosphere–asthenosphere boundary (LAB) beneath cratons. *Lithos* 109: 1–22.

Faber S and Müller G (1980) *Sp* phases from the transition zone between the upper and lower mantle. *Bulletin of the Seismological Society of America* 70: 487–508.

Farra V and Vinnik L (2000) Upper mantle stratification by *P* and *S* receiver functions. *Geophysical Journal International* 141: 699–712.

Farra V, Vinnik L, Romanowicz B, Kosarev GL, and Kind R (1991) Inversion of teleseismic *S* particle motion for azimuthal anisotropy in the upper mantle: A feasibility study. *Geophysical Journal International* 106: 421–431.

Fee D and Dueker K (2004) Mantle transition zone topography and structure beneath the Yellowstone hotspot. *Geophysical Research Letters* 31: L18603. http://dx.doi.org/10.1029/2004GL020636.

Ferris A, Abers GA, Christensen DH, and Veenstra E (2003) High resolution image of the subducted Pacific (?) plate beneath central Alaska, 50–150 km depth. *Earth and Planetary Science Letters* 214: 575–588.

Finotello M, Nyblade A, Julia J, Wiens D, and Anandakrishnan S (2011) Crustal V_p–V_s ratios and thickness for Ross Island and the Transantarctic Mountain front, Antarctica. *Geophysical Journal International* 185: 85–92.

Forgues E and Lambaré G (1992) Parameterization study for acoustic and elastic ray-Born inversion. *Journal of Seismic Exploration* 6: 253–277.

Frazer LN (1977) *Synthesis of Shear Coupled PL Waves*. PhD Thesis, Princeton University.

Frederiksen AW and Bostock MG (2000) Modelling teleseismic waves in dipping anisotropic structures. *Geophysical Journal International* 141: 401–412.

Frederiksen AW, Folsom H, and Zandt G (2004) Neighbourhood inversion of teleseismic Ps conversions for anisotropy and layer dip. *Geophysical Journal International* 155: 200–212.

Frederiksen AW and Revenaugh J (2004) Lithospheric imaging via teleseismic scattering tomography. *Geophysical Journal International* 159: 978–990.

French WS (1974) Two-dimensional and three-dimensional migration of model-experiment reflection profiles. *Geophysics* 39: 265–277.

Gilbert HJ, Sheehan AF, Dueker KG, and Molnar P (2003) Receiver functions in the western United States, with implications for upper mantle structure and dynamics. *Journal of Geophysical Research* 108: 2229. http://dx.doi.org/10.1029/2001JB001194.

Goldberg DE (1989) *Genetic Algorithms in Search, Optimization, and Machine Learning*. Reading, MA: Addison-Wesley.

Golub G, Heath M, and Wahba G (1979) Generalized cross-validation as a method for choosing a good ridge parameter. *Technometrics* 21: 215–223.

Gurrola H, Baker GE, and Minster JB (1995) Simultaneous time domain deconvolution with application to the computation of receiver functions. *Geophysical Journal International* 120: 537–543.

Gurrola H, Minster JB, and Owens T (1994) The use of velocity spectrum for stacking receiver functions and imaging upper mantle discontinuities. *Geophysical Journal International* 117: 427–440.

Haskell NA (1962) Crustal reflection of plane *P* and *SV* waves. *Journal of Geophysical Research* 67: 4751–4767.

Hayes MH, Lim JS, and Oppenheim AV (1980) Signal reconstruction from phase or magnitude. *IEEE Transactions on Acoustics, Speech, and Signal Processing* ASSP-28(6): 672–680.

Helffrich G and Thompson D (2010) A stacking approach to estimate V_P/V_S from receiver functions. *Geophysical Journal International* 182: 899–902.

Helmberger DV (1968) The crust-mantle transition in the Bering Sea. *Bulletin of the Seismological Society of America* 58: 179–214.

Hoffmann H, Boelsche J, Horst W, et al. (1989) Tiefenseismische untersuchungen in der DDR durch den VEB geophysik – Stand und ergebnisse. *Zeitschrift für Angewandte Geologie* 35: 308–314.

Hudson JA (1980) *The Excitation and Propagation of Elastic Waves*. New York, NY: Cambridge University Press.

Hudson JA and Heritage JR (1981) The use of the Born approximation in seismic scattering problems. *Geophysical Journal of the Royal Astronomical Society* 66: 221–240.

Jordan TH and Frazer LN (1975) Crustal and upper mantle structure from S_p phases. *Journal of Geophysical Research* 80: 1504–1518.

Kawakatsu H, Kumar P, Takei Y, et al. (2009) Seismic evidence for sharp lithosphere–asthenosphere boundaries of oceanic plates. *Science* 324: 499–502.

Kawakatsu H and Watada S (2007) Seismic evidence for deep water transportation in the mantle. *Science* 316: 1468–1471.

Kawakatsu H and Yoshioka S (2011) Metastable olivine wedge and deep dry cold slab beneath southwest Japan. *Earth and Planetary Science Letters* 303: 1–10.

Kennett BLN (1983) *Seismic Wave Propagation in Stratified Media*. Cambridge: Cambridge University Press.

Kennett BLN (1991) The removal of free surface interactions from three-component seismograms. *Geophysical Journal International* 104: 153–163.

Kennett BLN (2000) Stacking three-component seismograms. *Geophysical Journal International* 141: 263–269.

Kennett BLN (2002) *The Seismic Wavefield: Volume II. Interpretation of Seismograms on Regional and Global Scales*. New York, NY: Cambridge University Press.

Kind R, Kosarev GL, and Petersen NV (1995) Receiver functions at the stations of the German Regional Seismic Network (GRSN). *Geophysical Journal International* 121: 191–202.

Kind R and Vinnik LP (1988) The upper-mantle discontinuities underneath the GRF array from *P*-to-*SV* converted phases. *Journal of Geophysics* 62: 138–147.

Kind R, Yuan X, Saul J, et al. (2002) Seismic images of crust and upper mantle beneath Tibet: Evidence for Eurasian plate subduction. *Science* 298: 1219–1221.

Knapmeyer M and Harjes H-P (2000) Imaging crustal discontinuities and the downgoing slab beneath western Crete. *Geophysical Journal International* 143: 1–21.

Kosarev G, Kind R, Sobolev SV, Yuan X, Hanka W, and Oreshin S (1999) Seismic evidence for a detached Indian lithospheric mantle beneath Tibet. *Science* 283: 1306–1309.

Kosarev GL, Makeyeva LI, and Vinnik LP (1984) Anisotropy of the mantle inferred from observations of *P* to *S* converted waves. *Geophysical Journal of the Royal Astronomical Society* 76: 209–220.

Kosarev GL, Petersen NV, Vinnik LP, and Roecker SW (1993) Receiver functions for the Tien Shan analog broadband network: Contrasts in the evolution of structures across the Talasso-Fergana fault. *Journal of Geophysical Research* 98: 4437–4448.

Kumar MR and Bostock MG (2006) Transmission to reflection transformation of teleseismic wavefields. *Journal of Geophysical Research* 111: B08306.

Kumar MR and Bostock MG (2008) Extraction of absolute *P* velocity from receiver functions. *Geophysical Journal International* 175: 515–519.

Kumar P, Kind R, Hanka W, et al. (2005) The lithosphere–asthenosphere boundary in the North-West Atlantic region. *Earth and Planetary Science Letters* 1–2: 249–257.

Kurita T (1973) A procedure for elucidating fine structure of the crust and upper mantle from seismological data. *Bulletin of the Seismological Society of America* 63: 189–204.

Langston CA (1977) The effect of planar dipping structure on source and receiver responses for constant ray parameter. *Bulletin of the Seismological Society of America* 67: 1029–1050.

Langston CA (1979) Structure under Mt Rainier, Washington, inferred from teleseismic body waves. *Journal of Geophysical Research* 94: 1935–1951.

Langston CA and Hammer JK (2001) The vertical component P-wave receiver function. *Bulletin of the Seismological Society of America* 91: 1805–1819.

Lawrence JF and Wiens DA (2004) Combined receiver-function and surface wave phase-velocity inversion using a niching genetic algorithm: Application to Patagonia. *Bulletin of the Seismological Society of America* 94: 977–987.

Leidig M and Zandt G (2003) Highly anisotropic crust in the Altiplano Puna volcanic complex of the central Andes. *Journal of Geophysical Research* 108. http://dx.doi.org/10.1029/2001JB00649.

Levander A, Niu F, and Symes WW (2005) Imaging teleseismic *P* to *S* scattered waves using the Kirchhoff integral. In: Levander A and Nolet G (eds.). *Seismic Earth: Array Analysis of Broadband Seismograms*, vol. 157, pp. 149–169. Washington, DC: American Geophysical Union.

Levin V and Park J (1997) *P-SH* conversions in a flat-layered medium with anisotropy of arbitrary orientation. *Geophysical Journal International* 131: 253–266.

Levin V and Park J (1998) *P-SH* conversions in layered media with hexagonally symmetric anisotropy. A cookbook. *Pure and Applied Geophysics* 151: 669–697.

Li X-Q (1996) *Deconvolving Orbital Surface Waves for the Source Duration of Large Earthquakes and Modeling the Receiver Functions for the Earth Structure Beneath a Broadband Seismometer Array in the Cascadia Subduction Zone*. PhD Thesis, Oregon State University, Corvallis.

Li X, Kind R, Yuan X, Wolbern I, and Hanka W (2004) Rejuvenation of the lithosphere by the Hawaiian plume. *Nature* 427: 827–829.

Li X-Q and Nabelek JL (1999) Deconvolution of teleseismic body waves for enhancing structure beneath a seismometer array. *Bulletin of the Seismological Society of America* 89: 190–201.

Ligorria JP and Ammon CJ (1999) Iterative deconvolution and receiver-function estimation. *Bulletin of the Seismological Society of America* 89: 1395–1400.

Liu X and Pavlis GL (2013) Appraising the reliability of converted wavefield imaging: Application to USArray imaging of the 410-km discontinuity. *Geophysical Journal International* 49(3): 787–795. http://dx.doi.org/10.1093/gji/ggs088.

Lucente FP, Agostinetti NP, Moro M, Selvaggi G, and Di Bona M (2005) Possible fault plane in a seismic gap area of the southern Apennines (Italy) revealed by receiver function analysis. *Journal of Geophysical Research* 110: B04307. http://dx.doi.org/10.1029/2004JB003187.

Marfurt KJ, Johnson RA, and Pennington WD (2003) An introduction – Solid-earth seismology: Initiatives from IRIS. *The Leading Edge* 22: 218–219.

Matson KH (1997) *An Inverse-Scattering Series Method for Attenuating Elastic Multiples from Multicomponent Land and Ocean Bottom Seismic Data*. PhD Thesis, University of British Columbia, Vancouver.

Menke W (1984) *Geophysical Data Analysis: Discrete Inverse Theory*. Orlando, FL: Academic Press.

Mercier J-P, Bostock MG, and Baig A (2006) Improved Green's functions for passive source structural studies. *Geophysics* 71: SI95–SI102.

Miller DM, Oristaglio M, and Beylkin G (1987) A new slant on seismic imaging: Migration and integral geometry. *Geophysics* 52: 943–964.

Monteiller V, Chevrot S, Komatitsch D, and Fuji N (2013) A hybrid method to compute short-period synthetic seismograms of teleseismic body waves in a 3-D regional model. *Geophysical Journal International* 192: 230–247.

Muirhead KJ and Datt R (1976) The N-th root process applied to seismic array data. *Geophysical Journal of the Royal Astronomical Society* 47: 197–210.

Neal SL and Pavlis GL (1999) Imaging P to S conversions with multichannel receiver functions. *Geophysical and Research Letters* 26: 2581–2584.

Neal SL and Pavlis GL (2001) Imaging P to S conversions with broadband seismic arrays using mutichannel time-domain deconvolution. *Geophysical Journal International* 147: 57–67.

Nicholson T, Bostock M, and Cassidy JF (2005) New constraints on subduction zone structure in northern Cascadia. *Geophysical Journal International* 161: 849–859.

Niu F, Levander A, Ham S, and Obayashi M (2005) Mapping the subducting Pacific slab beneath southwest Japan with Hi-net receiver functions. *Earth and Planetary Science Letters* 239: 9–17.

Oppenheim AV and Schafer RW (1975) *Digital Signal Processing*. Englewood Cliffs, NJ: Prentice-Hall.

Oreshin S, Vinnik L, Peregoudov D, and Roecker S (2002) Lithosphere and asthenosphere of the Tien Shan imaged by S receiver functions. *Geophysical Research Letters* 29. http://dx.doi.org/10.1029/2001GL014441.

Owens TJ, Nyblade AA, Gurrola H, and Langston CA (2000) Mantle transition zone structure beneath Tanzania, east Africa. *Geophysical Research Letters* 27: 827–830.

Owens TJ and Zandt G (1997) The implications of crustal property variations on models of Tibetan Plateau evolution. *Nature* 387: 37–43.

Owens TJ, Zandt G, and Taylor SR (1984) Seismic evidence for an ancient rift beneath the Cumberland Plateau, Tennessee: A detailed analysis of broadband teleseismic P waveforms. *Journal of Geophysical Research* 89: 7783–7795.

Park J and Levin V (2000) Receiver functions from multiple-taper spectral correlation estimates. *Bulletin of the Seismological Society of America* 90: 1507–1520.

Park J and Levin V (2001) Receiver functions from regional *P* waves. *Geophysical Journal International* 147: 1–11.

Parker RL (1994) *Geophysical Inverse Theory*. Princeton, NJ: Princeton University Press.

Paulssen H, Visser J, and Nolet G (1993) The crustal structure from teleseismic, P-wave coda—I. Method. *Geophysical Journal International* 112: 15–25.

Pavlis GL (2005) Direct imaging of the coda of teleseismic P waves. In: Levander A and Nolet G (eds.). *Seismic Earth: Array Analysis of Broadband Seismograms*, vol. 157, pp. 171–185. Washington, DC: American Geophysical Union.

Phillips K, Clayton RW, Davis P, et al. (2012) Structure of the subduction system in southern Peru from seismic array data. *Journal of Geophysical Research* 117: B11306. http://dx.doi.org/10.1029/2012JB009540.

Phinney RA (1964) Structure of the Earth's crust from spectral behaviour of long-period body waves. *Journal of Geophysical Research* 69: 2997–3017.

Poppeliers C and Pavlis GL (2003a) Three-dimensional, prestack, plane wave migration of teleseismic *P*-to-*S* converted phases: 1. Theory. *Journal of Geophysical Research* 108. http://dx.doi.org/10.1029/2001JB000216.

Poppeliers C and Pavlis GL (2003b) Three-dimensional, prestack, plane wave migration of teleseismic *P*-to-*S* converted phases: 2. Stacking multiple events. *Journal of Geophysical Research* 108. http://dx.doi.org/10.1029/2001JB001583.

Press WH, Flannery BP, Teukolsky SA, and Vetterling WT (1986) *Numerical Recipes: The Art of Scientific Computing*. Cambridge: Cambridge University Press.

Randall GE (1989) Efficient calculation of differential seismograms for lithospheric receiver functions. *Geophysical Journal International* 99: 469–481.

Reading A, Kennett B, and Sambridge M (2003) Improved inversion for seismic structure using transformed *S*-wavector receiver functions: Removing the effect of the free surface. *Geophysical Research Letters* 30. http://dx.doi.org/10.1029/2003GL018090.

Revenaugh J (1995) A scattered-wave image of subduction beneath the Transverse Ranges, California. *Science* 268: 1888–1892.

Robinson E and Treitel S (1980) *Geophysical Signal Analysis*. Englewood Cliffs, NJ: Prentice-Hall.

Roecker S, Baker B, and McLaughlin J (2010) A finite-difference algorithm for full waveform teleseismic tomography. *Geophysical Journal International* 181: 1017–1040.

Rondenay S (2009) Upper mantle imaging with array recordings of converted and scattered teleseismic waves. *Surveys in Geophysics* 30: 377–405. http://dx.doi.org/10.1007/s10712-009-9071-5.

Rondenay S, Bostock MG, and Fischer KM (2005) Multichannel inversion of scattered teleseismic body waves: Practical considerations and applicability. In: Levander A and Nolet G (eds.) *Seismic Earth: Array Analysis of Broadband Seismograms*, vol. 157, pp. 187–203. Washington, DC: American Geophysical Union.

Rondenay S, Bostock MG, and Shragge J (2001) Multiparameter two-dimensional inversion of scattered teleseismic body waves, 3. Application to the Cascadia 1993 data set. *Journal of Geophysical Research* 106: 30795–30808.

Rost S and Thomas C (2002) Array seismology: Methods and applications. *Reviews of Geophysics* 40. http://dx.doi.org/10.1029/2000RG000100.

Ryberg T and Weber M (2000) Receiver function arrays: A reflection seismic approach. *Geophysical Journal International* 141: 1–11.

Rychert CA, Rondenay S, and Fischer KM (2007) *P*-to-*S* and *S*-to-*P* imaging of a sharp lithosphere–asthenosphere boundary beneath eastern North America. *Journal of Geophysical Research* 112: B08314. http://dx.doi.org/10.1029/2006JB004619.

Rychert CA, Shearer P, and Fischer KM (2010) Scattered wave imaging of the lithosphere–asthenosphere boundary. *Lithos* 120: 173–185.

Sacks IS, Snoke JA, and Husebye ES (1979) Lithosphere thickness beneath the Baltic shield. *Tectonophysics* 56: 101–110.

Sambridge M (1999a) Geophysical inversion with a neighbourhood algorithm—I. Search a parameter space. *Geophysical Journal International* 138: 479–494.

Sambridge M (1999b) Geophysical inversion with a neighbourhood algorithm—II. Appraising the ensemble. *Geophysical Journal International* 138: 727–746.

Saul J, Kumar MR, and Sarkar D (2000) Lithospheric and upper mantle structure of the Indian Shield, from teleseismic receiver functions. *Geophysical Research Letters* 27: 2357–2360.

Schaeffer AJ and Bostock MG (2010) A low-velocity zone atop the transition zone in northwestern Canada. *Journal of Geophysical Research* 115: B06302. http://dx.doi.org/10.1029/2009JB006856.

Schimmel M and Paulssen H (1997) Noise reduction and the detection of weak, coherent signals through phase-weighted stacks. *Geophysical Journal International* 130: 497–505.

Schneider WS (1978) Integral formulation for migration in two and three dimensions. *Geophysics* 43: 49–76.

Schulte-Pelkum V, Monsalve G, Sheehan A, et al. (2005) Imaging the Indian subcontinent beneath the Himalaya. *Nature* 435: 1222–1225.

Sheehan AF, Shearer PM, Gilbert HJ, and Dueker KG (2000) Seismic migration processing of *P-SV* converted phases for mantle discontinuity structure beneath the Snake River Plain, western United States. *Journal of Geophysical Research* 105: 19055–19065.

Sherwood JWC and Trorey AW (1965) Minimum-phase and related properties of a horizontally stratified absorptive Earth to plane acoustic waves. *Geophysics* 30: 191–197.

Shibutani T, Sambridge M, and Kennett BLN (1996) Genetic algorithm inversion for receiver functions with application to crust and uppermost mantle structure beneath eastern Australia. *Geophysical Research Letters* 23: 1829–1832.

Shragge J, Bostock MG, and Rondenay S (2001) Multiparameter two-dimensional inversion of scattered teleseismic body waves, 2. Numerical examples. *Journal of Geophysical Research* 106: 30783–30794.

Silver PG and Chan WW (1991) Shear-wave splitting and subcontinental mantle deformation. *Journal of Geophysical Research* 96: 16429–16454.

Silver PG and Savage M (1994) The interpretation of shear-wave splitting parameters in the presence of two anisotropic layers. *Geophysical Journal International* 119: 949–963.

Simmons NA and Gurrola H (2000) Multiple seismic discontinuities near the base of the transition zone in the Earth's mantle. *Nature* 405: 559–562.

Stammler K, Kind R, Petersen N, Kosarev G, Vinnik LP, and Qiyuan L (1992) The upper mantle discontinuities: Correlated or anticorrelated? *Geophysical Research Letters* 19: 1563–1566.

Svenningsen L and Jacobsen BH (2004) Comment on "Improved inversion for seismic structure using transformed, *S*-wavevector receiver functions: Removing the effect of the free surface" by Anya Reading, Brian Kennett, and Malcolm Sambridge. *Geophysical Research Letters* 31: L24609. http://dx.doi.org/10.1029/2004GL021413.

Tarantola A (1984) Inversion of seismic reflection data in the acoustic approximation. *Geophysics* 49: 1259–1266.

Tarantola A (1986) A strategy for nonlinear elastic inversion of seismic reflection data. *Geophysics* 51: 1893–1903.

Thomson DJ (1982) Spectrum estimation and harmonic analysis. *Proceedings of IEEE* 70: 1055–1096.

Thorwart M and Dahm T (2005) Wavefield decomposition for passive ocean bottom seismological data. *Geophysical Journal International* 163: 611–621.

Tromp J, Tape C, and Liu Q (2005) Seismic tomography, adjoint methods, time reversal and banana-doughnut kernels. *Geophysical Journal International* 160: 195–216.

Ulrych TJ (1971) Application of homomorphic deconvolution to seismology. *Geophysics* 36: 650–660.

Ulrych TJ, Jensen OG, Ellis RM, and Somerville PG (1972) Homomorphic deconvolution of some teleseismic events. *Bulletin of the Seismological Society of America* 62: 1269–1281.

Vinnik LP (1977) Detection of waves converted from *P* to *SV* in the mantle. *Physics of the Earth and Planetary Interiors* 15: 39–45.

Vinnik LP, Farra V, and Romanowicz B (1989) Azimuthal anisotropy in the earth from observations of *SKS* at GEOSCOPE and NARS broad band stations. *Bulletin of the Seismological Society of America* 79: 1542–1558.

Vinnik LP, Foulger GR, and Du Z (2005) Seismic boundaries in the mantle beneath Iceland: A new constraint on temperature. *Geophysical Journal International* 160: 533–538.

Vinnik LP and Montagner J-P (1996) Shear-wave splitting in the mantle *Ps* phases. *Geophysical Research Letters* 23: 2449–2452.

Vinnik L and Romanowicz B (1991) Origin of precursors to teleseismic *S* waves. *Bulletin of the Seismological Society of America* 81: 1216–1230.

Wapenaar K, Thorbecke J, and Draganov D (2004) Relations between reflection and transmission responses of three-dimensional inhomogeneous media. *Geophysical Journal International* 156: 179–194.

Weglein AB, Araújo FV, Carvalho PM, et al. (2003) Inverse scattering series and seismic exploration. *Inverse Problems* 19: R27–R83.

Weglein AB, Foster DJ, Matson KH, Shaw SA, Carvalho PM, and Corrigan D (2002) Predicting the correct spatial location of reflectors without knowing or determining the precise medium and wave velocity: Initial concept, algorithm and analytic and numerical example. *Journal of Seismic Exploration* 10: 367–382.

Weglein AB, Gasparotto FA, Carvalho PM, and Stolt RH (1997) An inverse scattering series method for attenuating multiples in seismic reflection data. *Geophysics* 62: 1975–1989.

Wei Z, Chen L, and Xu W (2011) Crustal thickness and V_p/V_s ratio of the central and western North China Craton and its tectonic implications. *Geophysical Journal International* 186: 385–389.

Wilson DC, Angus DA, Ni JF, and Grand S (2006) Constraints on the interpretation of *S*-to-*P* receiver functions. *Geophysical Journal International* 165: 969–980.

Wilson D and Aster R (2005) Seismic imaging of the crust and upper mantle using regularized joint receiver functions, frequency P-wave number filtering, and multimode Kirchhoff migration. *Journal of Geophysical Research* 110: B05305. http://dx.doi.org/10.1029/2004JB003430.

Wilson D, Aster R, Ni J, et al. (2005) Imaging the seismic structure of the crust and upper mantle beneath the Great Plains, Rio Grande Rift, and Colorado Plateau using receiver functions. *Journal of Geophysical Research* 110: B05306. http://dx.doi.org/10.1029/2004JB003492.

Wilson CK, Jones CH, Molnar P, Sheehan AF, and Boyd OS (2004) Distributed deformation in the lower crust and upper mantle beneath a continental strike-slip fault zone: Marlborough fault system, South Island, New Zealand. *Geology* 32: 837–840.

Wittlinger G and Farra V (2012) Observation of low shear wave velocity at the base of the polar ice sheets: Evidence for enhanced anisotropy. *Geophysical Journal International* 190: 391–405.

Wittlinger G, Farra V, Hetényi G, Vergne J, and Nábèlek J (2009) Seismic velocities in Southern Tibet lower crust: A receiver function approach for eclogite detection. *Geophysical Journal International* 177: 1037–1049.

Yilmaz O (2001) *Seismic Data Analysis: Processing, Inversion, and Interpretation of Seismic Data*. Tulsa, OK: Society of Exploration Geophysicists.

Yuan X, Kind R, Li X, and Wang R (2006) The *S* receiver functions: Synthetics and data examples. *Geophysical Journal International* 165: 555–564.

Zandt G and Ammon C (1995) Continental crust composition constrained by measurements of crustal Poisson's ratio. *Nature* 374: 152–154.

Zandt G, Gilbert H, Owens TJ, Ducea M, Saleeby J, and Jones CH (2004) Active foundering of a continental arc root beneath the southern Sierra Nevada in California. *Nature* 431: 41–46.

Zandt G and Owens TJ (1986) Comparison of crustal velocity profiles determined by seismic refraction and teleseismic methods. *Tectonophysics* 128: 155–161.

Zandt G and Randall GE (1985) Observations of shear-coupled *P* waves. *Geophysical Research Letters* 12: 565–568.

Zhou L, Chen W-P, and Özalaybey S (2000) Seismic properties of the central Indian Shield. *Bulletin of the Seismological Society of America* 90: 1295–1304.

Zhu L and Kanamori H (2000) Moho depth variation in southern California from teleseismic receiver functions. *Journal of Geophysical Research* 105: 2969–2980.